

New CAD Models for Spiral Inductors and EM Coupling for EM Based Circuit Design

Navid Arbabi

A Thesis
in
the Department
of
Electrical and Computer Engineering

Presented in Partial Fulfillment of the Requirements
for the Degree of Master of Applied Science (Electrical and Computer Engineering) at

Concordia University
Montreal, Quebec, Canada

July 2008

©Navid Arbabi, 2008



Library and
Archives Canada

Bibliothèque et
Archives Canada

Published Heritage
Branch

Direction du
Patrimoine de l'édition

395 Wellington Street
Ottawa ON K1A 0N4
Canada

395, rue Wellington
Ottawa ON K1A 0N4
Canada

Your file Votre référence
ISBN: 978-0-494-42490-2
Our file Notre référence
ISBN: 978-0-494-42490-2

NOTICE:

The author has granted a non-exclusive license allowing Library and Archives Canada to reproduce, publish, archive, preserve, conserve, communicate to the public by telecommunication or on the Internet, loan, distribute and sell theses worldwide, for commercial or non-commercial purposes, in microform, paper, electronic and/or any other formats.

The author retains copyright ownership and moral rights in this thesis. Neither the thesis nor substantial extracts from it may be printed or otherwise reproduced without the author's permission.

AVIS:

L'auteur a accordé une licence non exclusive permettant à la Bibliothèque et Archives Canada de reproduire, publier, archiver, sauvegarder, conserver, transmettre au public par télécommunication ou par l'Internet, prêter, distribuer et vendre des thèses partout dans le monde, à des fins commerciales ou autres, sur support microforme, papier, électronique et/ou autres formats.

L'auteur conserve la propriété du droit d'auteur et des droits moraux qui protègent cette thèse. Ni la thèse ni des extraits substantiels de celle-ci ne doivent être imprimés ou autrement reproduits sans son autorisation.

In compliance with the Canadian Privacy Act some supporting forms may have been removed from this thesis.

Conformément à la loi canadienne sur la protection de la vie privée, quelques formulaires secondaires ont été enlevés de cette thèse.

While these forms may be included in the document page count, their removal does not represent any loss of content from the thesis.

Bien que ces formulaires aient inclus dans la pagination, il n'y aura aucun contenu manquant.

■*■
Canada

ABSTRACT

New CAD Models for Spiral Inductors and EM Coupling for EM Based Circuit Design

Navid Arbabi

This thesis contributes several techniques for electromagnetic-based computer-aided modeling, design, optimization and simulation of RF/microwave components and circuits.

First, computer-aided design (CAD) of spiral inductors exploiting full-wave electromagnetic (EM) analysis is proposed. Traditional optimization methods for spiral inductors rely on circuit models and they are inaccurate compared to EM simulations. Space-mapping optimization combines the speed of circuit models and the accuracy of EM simulations. A space-mapping optimization algorithm is proposed which yields an EM-validated spiral inductor design/layout with considerable improvement over those obtained by traditional optimization methods.

Second, a very compact composite low-pass filter is presented. It offers good matching properties in the pass-band and features an attenuation pole near the cutoff frequency leading to a sharper attenuation response. The filter is implemented using spiral inductors and metal-insulator-metal capacitors. The filter occupies a compact area of $1.4\text{mm}\times 0.8\text{mm}$ which is much smaller than other filters operating in the same frequency range.

The measured response of the overall circuit might not match or could be entirely different from the expected response, even if the passive components are designed accurately. This is because coupling between components can play an important role in the circuit performance especially in dense circuits. An efficient and recent CAD model for EM coupling, previously applied to passive EM circuit simulation, is considered. This CAD technique is applied to EM coupling modeling of a nonlinear RFIC consisting of both active and passive components. The efficiency of the technique is demonstrated through an amplifier circuit simulation.

Acknowledgements

First of all, I would like to express my sincere appreciation for my research advisors, Dr. Vijay Devabhaktuni and Dr. M.C.E. Yagoub, for their tireless efforts, continued guidance and encouragement during completion of this work. Inspirations drawn from the fruitful and enlightening technical discussions with them have been crucial in making this project successful.

I would also like to express my appreciation to Dr. Don Davis (part-time faculty in the ECE department of Concordia) for his valuable advices on chapter 3 of this thesis. Additionally, this work would not have been possible without the efforts and support of the current and previous members of Concordia CAD modeling and design group, Li Zhu, Arash Kashi, Mani Najmabadi, Farzin Manoucheri, Kaustubha Mendhurwar, Joshua Frankel, Niladri Roy, Rajasekhar Kakumani, and Ahmad Zbeeb.

Lastly I'd like to extend my heartfelt appreciation to my parents, Azizeh and Ahmad, whose ongoing guidance, support, and understanding gave me the strength to finish this work.

*To my loving parents
Azizeh & Ahmad*

Table of Contents

List of Figures	ix
List of Tables	xii
List of Symbols and Abbreviations	xiii
Chapter 1 Introduction	1
1.1. Motivation and Objectives	1
1.1.1. Design/Optimization of Spiral Inductors	2
1.1.2. Design/Optimization of Composite Low-Pass Filters	4
1.1.3. EM Coupling Model for Active Circuit Simulation	6
1.2. Scope and Organization	8
Chapter 2 Design/Optimization of Spiral Inductors Applying Space Mapping	
Algorithm	10
2.1. Background and Motivation	10
2.2. Different Types of Spiral Inductors.....	13
2.3. Spiral Inductor Circuit Model and Related Formulations.....	14
2.3.1. Inductance Calculation	16
2.3.2. Quality Factor	18
2.4. Space Mapping Technology	21
2.4.1. Space Mapping (SM) Concept.....	21
2.4.2. Implicit Space Mapping (ISM)	23
2.5. Proposed SQP Based SM Algorithm for Spiral Inductor optimization.....	25
2.5.1. Parameter Extraction.....	25
2.5.2. Optimization Objective.....	27
2.6. Example of Spiral Inductor Design/Optimization.....	29
2.7. Summary.....	31
Chapter 3 Design of a Compact Composite Low-Pass Filter	32
3.1. Background and Motivation.....	32
3.2. Composite Filter Design by the Image Parameter Method.....	34

3.2.1.	Image Impedances and Transfer Functions for Two-Port Networks	35
3.2.2.	Constant- k Filter Sections	39
3.2.3.	m -Derived Filter Sections.....	42
3.2.4.	Composite Filters	48
3.2.5.	A Composite LPF Design Example	49
3.3.	Compact Realization of the Designed LPF and Full Wave Simulation Results	52
3.3.1.	Choice of Substrate and Metal Layers	52
3.3.2.	Design/Optimization of Inductors and Capacitors	53
3.3.3.	Design/Optimization of Resonators	55
3.3.4.	Simulation Results of the Composite LPF	56
3.4.	Summary	59
Chapter 4 Nonlinear Circuit Simulation Using EM Coupling CAD Model.....		60
4.1.	Background and Motivation.....	60
4.2.	Characteristic Matrices and their Properties	62
4.2.1.	Scattering Parameter Matrices.....	62
4.2.2.	Transfer Matrix.....	63
4.3.	Review of the Coupling Model Technique	65
4.4.	Application to Nonlinear Simulation	68
4.5.	Summary	75
Chapter 5 Conclusions		76
References.....		80

List of Figures

Figure 2.1. On-chip spiral inductor realizations: (a) square, (b) hexagonal, (c) octagonal, and (d) circular	13
Figure 2.2. Cross-section of a spiral inductor [36].....	14
Figure 2.3. Equivalent circuit model of the spiral inductor [5].....	15
Figure 2.4. Equivalent circuit model of the spiral inductor with one end connected to the ground [40].....	20
Figure 2.5. Overview of space mapping [23].....	23
Figure 2.6. Basic concept of the ISM technique [21].....	24
Figure 2.7. Flow-chart of the proposed SQP based space mapping algorithm	29
Figure 3.1. A two-port network terminated in its image impedances	35
Figure 3.2. A two-port network terminated in its image impedances and driven with a voltage generator.....	37
Figure 3.3. Low-pass constant- k filter sections in T and π form. (a) T -section. (b) π -section.....	39
Figure 3.4. Typical passband and stopband characteristic of the low-pass constant- k sections of Fig. 3.3	41
Figure 3.5. Development of an m -derived filter section from a constant- k section. (a) Constant- k section. (b) General m -derived section. (c) Final m -derived section.....	42
Figure 3.6. Low-pass m -derived T filter section	43
Figure 3.7. Typical attenuation responses for constant- k , m -derived, and composite filters	44
Figure 3.8. Development of an m -derived π -section. (a) Infinite cascade of m -derived T -sections. (b) A de-embedded π -equivalent.....	45

Figure 3.9. Variation of Z_{in} in the passband of a low-pass m -derived section for different values of m	46
Figure 3.10. A bisected π -section used to match Z_{in} to Z_{iT}	47
Figure 3.11. (a) Design concept and (b) schematic of a composite LPF.....	48
Figure 3.12. (a) Lumped equivalent circuit representation of the composite LPF. (b) The corresponding S -parameter responses.....	51
Figure 3.13. Cross-section of (a) spiral inductor and (b) MIM capacitor.....	53
Figure 3.14. Top view of (a) spiral inductor and (b) MIM capacitor	53
Figure 3.15. (a) A series LC resonator and (b) corresponding EM simulations.....	55
Figure 3.16. Layout of the proposed composite LPF in Zeland $IE3D$	57
Figure 3.17. S -parameter responses of the proposed composite LPF obtained from EM simulations (Zeland $IE3D$) and ideal model simulations (Agilent ADS).....	58
Figure 4.1. A two port network representation with the related incident and reflected waves.....	63
Figure 4.2. (a) Original circuit, in which, $[T_A]$ and $[T_B]$ are the transfer matrices of components A and B respectively and $[T_I]$ is the transfer matrix of interconnect I .(b) Modified topology [10], which includes EM coupling between components denoted by $[T_{X1}]$ and $[T_{X2}]$ respectively	65
Figure 4.3. Series RLC circuit considered in [10] for demonstrating the usefulness of the coupling algorithm	67
Figure 4.4. Comparison of magnitudes and phases of the scattering parameters S_{11} and S_{12} computed using the recent coupling algorithm [10] with those obtained from a time-consuming direct overall circuit simulation in Sonnet em	68
Figure 4.5. (a) ADS schematic and (b) Momentum layout of the power amplifier.....	70

Figure 4.6. Frequency spectra of the output signal corresponding to (a) input power = -20dBm and (b) input power = -3 dBm. Time-domain waveforms of the output signal corresponding to (c) input power = -20dBm and (d) input power = -3dBm.....	71
Figure 4.7. Output power <i>versus</i> input power of the power amplifier	71
Figure 4.8. Comparison of magnitudes and phases of the scattering parameters S_{21} and S_{22} computed using the recent coupling algorithm both without coupling (.) and with coupling (Δ), with those obtained from time-consuming direct overall circuit-level simulation (—).....	74

List of Tables

Table 2.1 Coefficients for Modified Wheeler Expression.....	17
Table 2.2 Coefficients for Current Sheet Expression	17
Table 2.3 Coefficients for Data-Fitted Monomial Expression	18
Table 2.4 Constraints on Design Parameters	30
Table 2.5 Comparison of Inductor Optimization Algorithms	31
Table 3.1 Image Parameters for T and π Networks	38
Table 3.2 Theoretical Expressions and Values of the Lumped Elements ($f_c = 2.8$ GHz and $R_0 = 50 \Omega$).....	50
Table 3.3 Dimensions of Spiral Inductors in the Proposed Composite LPF	57
Table 3.4 Dimensions of MIM Capacitors in the Proposed Composite LPF	57
Table 3.5 Comparison of the Performances of the Proposed Filter Obtained Using Ideal Model and Full-Wave Simulations	58

List of Symbols and Abbreviations

ASM	aggressive space mapping
BPF	band-pass filter
C_{ox}	oxide capacitance between the spiral and the substrate
C_s	direct coupling through the overlap between the spiral and the underpass
C_{si}	capacitance of silicon substrate
C_{sub}	substrate capacitance per unit area
CAD	computer aided design
d_{avg}	average diameter of spiral inductor
d_{in}	inner diameter of spiral inductor
d_{out}	outer diameter of spiral inductor
EM	electromagnetic
f	frequency
f_c	cutoff frequency
FoM	figure of merit
G_{sub}	substrate conductance per unit area
GP	geometric programming
ISM	implicit space mapping
l	total length of spiral
L_s	inductance of the spiral inductor
LNA	low noise amplifier
LPF	low-pass filter
MADS	mesh adaptive direct search

MCM	multi chip module
MIM	metal-insulator-metal
MMIC	monolithic microwave integrated circuit
N	number of turns of spiral inductor
OSM	Output space mapping
PE	parameter extraction
Q	quality factor
R_c	response vector of coarse model
R_f	response vector of fine model
R_0	nominal characteristic impedance
R_s	resistance of the metal trace of spiral inductor
R_{si}	resistance of silicon substrate
RF	radio frequency
RFIC	radio frequency integrated circuit
s	turn spacing of spiral inductor
SM	space mapping
SoC	system on chip
SQP	sequential quadratic programming
t	metal thickness
t_{ox}	oxide thickness between the spiral and the substrate
$t_{ox\ M1-M2}$	oxide thickness between the spiral and the underpass
VCO	voltage controlled oscillator
w	turn width of spiral inductor

\mathbf{x}_c	coarse model design parameters
\mathbf{x}_f	fine model design parameters
$Z_{i\pi}$	image impedance of the low-pass π -network
Z_{iT}	image impedance of the low-pass T -network
δ	metal skin depth
μ_0	free space permeability
ϵ_{ox}	oxide permittivity
ρ	fill ratio of spiral inductor
σ	metal conductivity

Chapter 1

Introduction

1.1 Motivation and Objectives

Currently, the industry is leading towards higher integration where large designs are integrated onto a single die, referred to as System on a Chip (SoC). Higher integration has the advantages of increased performance and reduced costs, but the die size must remain small enough to maintain high yields. Therefore, design of compact components and circuits is an important and challenging research area. Knowing that die area is crucial for yield and SoC design, current research has explored the use of lumped elements for Monolithic Microwave Integrated Circuits (MMIC). Lumped elements consume much less die area than distributed elements which are conventionally used in circuits such as filters. The use of lumped elements materializes large savings in terms of die area at the cost of slightly degraded results and higher power consumption.

Lumped elements at GHz frequencies are also extensively used in Multi Chip Modules (MCMs) [1]. MCMs mount multiple chips inside a single package, and can incorporate

many lumped elements. Therefore, MCM can reduce the overall footprint of a circuit on the motherboard compared to single chip approaches. As such, lumped elements possess an edge over distributed elements as they consume less area which is very crucial in the MCM.

In the light of the above discussion, this thesis addresses three important issues pertaining to the compact design of RF/Microwave components and circuits. First, design and optimization of spiral inductors as an example of compact component design using lumped elements is studied. Spiral inductors are considered since they are attractive candidates in the implementation of inductors as lumped elements in GHz frequencies. Second, the design and optimization of an ultra compact low-pass filter for MMIC applications is discussed, as an example of compact circuit design using lumped elements. Overall circuits assembled using precisely designed passive components (*e.g.* spiral inductors) could fail to match the expected response or could produce an entirely different response. This is because interactions between components can play an important role in the circuit performance especially in dense circuits. Therefore, finally, a technique that models these interaction effects in dense circuits is studied and applied to passive and active circuit simulation.

1.1.1 Design/Optimization of Spiral Inductors

Portable wireless communication equipment requires low-cost, high level integration, and high-performance Radio Frequency Integrated Circuits (RFIC). Silicon technology is currently the most suitable candidate due to the ongoing improvements in processing

technologies that have continually enhanced the Radio Frequency (RF) performance of silicon-based transistors [2][3]. Exploitations of silicon technologies require the availability of optimized integrated inductors with high quality factors (Q) to enhance the performance of RF circuits. This is due to the influence of the spiral inductor on the performance of many RF circuits. One example is the bandpass filter (BPF) built with inductors and capacitors, in which the Q of the spiral inductor determines the insertion loss [4]. In low noise amplifiers (LNA), the Q of the spiral inductor determines the figure of merit (FoM), which is the measure of the overall performance of the LNA [4]. In voltage controlled oscillators (VCO), high- Q spiral inductors reduce both DC power consumption and phase noise [4].

Several methods have been proposed to model spiral inductors on silicon. They can be divided into two categories. One of the categories uses compact circuit models such as physically based circuit models [5][6], empirical circuit models [7][8], or circuit models which are constructed by calculating the effect of each segment of the spiral inductor and the interconnection between them [9]. The other category solves Maxwell's equations, using electromagnetic simulators, such as Ansoft HFSS [10], Sonnet em [11] and Agilent Momentum [12].

Synthesis and optimization of spiral inductors on silicon has also been studied at the same time. Most of the work in this area is based on circuit models. Some examples are an analytical design procedure [13] based on the physical model, geometric programming (GP) formulation of the spiral inductor optimization [14][15] based on the model

presented by S.S. Mohan *et al.* [8], sequential quadratic programming (SQP) [16] and an optimization method called mesh adaptive direct search (MADS) [17]. These methods are very efficient but the accuracies of the optimized spiral inductor designs are limited by the circuit model approximations. It is likely that the design does not meet the specification when validated by electromagnetic (EM) simulators or measurements. On the other hand, direct optimization based on EM simulators offers accurate results but it is computationally very expensive and time-consuming. To address this problem, Bandler *et al.* introduced space mapping (SM) technology [18]-[23] in 1994 to incorporate the computational efficiency of cheap circuit models and the accuracy of expensive EM simulations. Space mapping algorithms perform optimization on a computationally cheap circuit model and use EM simulations to calibrate the circuit model.

The work presented in chapter 2 of this thesis focuses on a space-mapping algorithm for the design/optimization of on-chip spiral inductors. The proposed Computer Aided Design (CAD) algorithm is demonstrated through a practical spiral inductor optimization example. EM-validated designs can be obtained by the proposed method in minutes or hours instead of days and weeks as in the case of conventional methods.

1.1.2 Design/ Optimization of Composite Low-Pass Filters

Compact circuit design using lumped elements is studied in the second step. To this end design and optimization of an ultra compact low-pass filter for MMIC applications is discussed. In most microwave communication systems, filters play an extremely important role. Microwave filters are used to control the frequency response in a

microwave system by providing transmission at frequencies within the passband and attenuation in the stopband. Filters are used in electrical engineering to shape the signal, which is especially crucial in reducing input signal noise in receivers and spurious emissions in transmitters. Microwave filters have traditionally been built using waveguides and coaxial lines. Recent microwave printed filters have unique advantages over waveguide and coaxial filters in terms of low cost, high accuracy, and compact size. Another advantage of printed filters is their easy integration with active circuits (*i.e.*, filters can be fabricated on the same substrate with transistor amplifiers, oscillators, and other active circuits).

Applications such as wireless communications continue to challenge microwave filter designers with increasingly strict requirements such as higher performance, higher selectivity, smaller size, etc. The work presented in chapter 3 of this thesis focuses on the desire to effectively reduce the volume and increase the selectivity of printed low-pass filters (LPF). Therefore the objective of the work is to implement a planar LPF with relatively more compact size and higher selectivity than traditional planar LPFs. To this end composite LPF design approach [24][25] is applied. This design approach leads to a LPF schematic which requires lower order to achieve a very sharp cutoff response and good matching properties in the passband as compared to conventional design approaches such as Butterworth, Chebyshev, and elliptic LPFs. The lower order of the composite filter makes the design more compact and less expensive due to the reduced number of elements in the design. To keep the circuit ultra compact, spiral inductors and metal-

insulator-metal (MIM) capacitors are employed for implementation of lumped elements, which makes the filter suitable for MMIC applications.

1.1.3 EM Coupling Model for Active Circuit Simulation

The use of lumped elements at high frequencies is extremely important to emerging technologies like SoCs and MCMs, but it is subject to high parasitic and electromagnetic (EM) coupling. Coupling is a general term used to describe EM field interactions between two structures. Distributed and mutual coupling, which result from EM field interactions in the network, exert a significant effect on integrated circuits [26]. This parasitic effect can become more of a concern in SoCs and MCMs as packing densities of components are increased and frequencies are pushed even higher [27]. For instance in a densely packed MIC amplifier using lumped elements, coupling can cause the centre frequency and magnitude to shift significantly depending on the layout and frequency of operation. Although such unintended coupling between components plays an important role in the circuit performance, this quantity is very complex to evaluate. Existing lumped or physical/geometrical-based models do not adequately include all EM effects. On the other hand, although EM-based models are accurate, they cannot be easily implemented in a circuit simulator and are time consuming to generate. Until recently, it has been practiced to effectively ignore EM coupling in lumped elements since the effect is less prominent at the lower side of the microwave spectrum. However, with the increase of operating frequencies up to the millimeter range, new designs using lumped elements instead of distributed elements have been presented at frequencies higher than

40 GHz where EM effects can be significant [26]. These include, for instance, a 50GHz Mixer by Dickson [28], and a 52 GHz LNA by Gordon [29].

Recently, several techniques in bringing the coupling phenomenon forward into the circuit design have been investigated [26][30][31][32]. The coupling phenomenon exists at such a high frequency that full wave EM simulators are required which are primarily based on the solution of Maxwell's equations to quantify the EM field in a structure. These simulators are accurate but require huge computation time and memory space. This aspect is crucial when modern CAD tools lead to massive and highly repetitive computational tasks during simulation, optimization and statistical analysis. As such, development of fast and full EM representations with high-order coupling is crucial for modern circuit design. Furthermore, existing lumped element EM-based models have an important drawback at the circuit level. Although these models are accurate, they are developed in a perfectly shielded environment, *i.e.*, excluding any external effects such as coupling with neighbouring components.

Quite recently, a novel EM coupling CAD modeling technique based on simple network theory concepts and de-embedding techniques [33] has been proposed [34]. The accuracy and efficiency of the modeling technique has been demonstrated for a variety of passive circuits. Since active devices (*e.g.* transistors) are widely used in RFICs (*e.g.* power amplifiers), in chapter 3 of this thesis the CAD modeling technique [34] is applied for the first time to nonlinear circuit simulation. Accurate and fast circuit-level simulations are obtained.

1.2 Scope and Organization

The following is the scope of research work in this thesis:

- Applying implicit space mapping technology to the optimization of spiral inductors.
- Developing a parameter extraction scheme with few preassigned parameters leading to better convergence in the spiral inductor optimization process.
- Designing a compact composite LPF using spiral inductors and MIM capacitors.
- Extending the application of a recent, fast and efficient method to model EM coupling in microwave integrated passive/active circuits.

The thesis is organized as follows:

In chapter 2, a review of a physically based circuit model of spiral inductors [6] and the development of space mapping technology, focusing on the implicit space mapping (ISM) [21] is presented. Space mapping technology is then applied to the optimization of spiral inductors. The proposed CAD algorithm is demonstrated through a practical spiral inductor optimization example and an EM-validated design of a spiral inductor is obtained in five full-wave EM simulations.

In chapter 3, a review of the image parameter method to design composite LPFs [24][25] is discussed. A composite LPF is designed and realised by spiral inductors and MIM capacitors. Satisfactory EM simulation results are obtained and presented.

In chapter 4, a review of the new coupling modeling technique [34] is presented. A passive circuit simulation example applying the coupling model is also discussed.

Considerations for applying the model for circuits containing active components are given. Finally, an active circuit more specifically an amplifier simulation applying the coupling model is presented.

Finally, chapter 5 draws conclusions and discusses possible contributions of this work leading to future research.

Chapter 2

Design/Optimization of Spiral

Inductors Applying Space Mapping

Algorithm

2.1 Background and Motivation

Several electronic circuits, *e.g.* LNAs, VCOs, filters etc., require inductors with high quality-factors (Q). At GHz frequencies, several effects including eddy current, self resonance, skin effect, and substrate loss degrade the Q of the inductor. The magnitude of each of these effects depends strongly on the layout and physical dimensions of the inductor. As such, CAD and optimization of on-chip spiral inductors can be challenging.

The main objective in the design of spiral inductors is to come up with a design/layout which achieves high- Q at a specified inductance (L). Several methods have been proposed in the RF/microwave literature. Exhaustive enumeration [35] first discretizes

the geometrical parameters within the design space of interest. Then, for each of the combinations of the resulting parameter values, inductor performance is simulated. Finally, those parameter values resulting in the highest Q are recommended for fabrication. Such an approach can be viewed as a “trial-and-error” approach, and the CPU-time required is exponential with respect to the number of the design variables. Geometric programming [14] is yet another commonly used optimization technique. However, this technique demands that the coarse model be in a specific format (*i.e.* posynomial functions), thereby limiting its applicability. For instance, on-chip spiral inductors may not necessarily follow posynomial input-output relationships. Sequential quadratic programming (SQP) has recently emerged as an alternative vehicle to inductor optimization. In [16], EM effects, *e.g.* substrate effects, were neglected for simplifying the SQP based inductor optimization. Consequently, the resulting designs miss the critical high-frequency effects. In general, all the above-mentioned optimization tools based on circuit models (*i.e.* coarse models with limited accuracies) of spiral inductors do not use EM data. The accuracies of the optimized spiral inductor designs are hence limited by the circuit model approximations. On the other hand, EM simulators such as *Sonnet em* [11] or Ansoft *HFSS* [10] offer accurate models for spiral inductors. However, they are usually CPU-intensive and direct optimization is usually impractical, if not impossible.

Space-mapping (SM) [18] has recently emerged as an efficient engine for EM based optimization of passive components. SM is a mathematical tool, which combines the

speed of “coarse models” (approximate circuit-based models or empirical models) with the accuracy of “fine models” (CPU-intensive EM solvers) to enable accurate yet fast EM based optimization solutions. It is to be noted that the convergence of SM based CAD tools (including those used for inductor design) depends both on the accuracy of the coarse models and the techniques used for coarse model optimization.

A space-mapping tool based on geometric programming for design/optimization of spiral inductors has been recently introduced in [36]. The approach involves defining iteration-dependent constraints in the parameter extraction (PE) step. Without suitable constraints, the surrogate model resulting from this approach may critically diverge from the coarse model and hence the design solution obtained may not be a close approximation of the fine model optimum.

In this chapter, an SQP based space-mapping algorithm for the design/optimization of on-chip spiral inductors is proposed and formulated. After reviewing different types of spiral inductors, a physically-based circuit model of spiral inductor is discussed. Following this, the basic concept of space mapping technology, focusing on the implicit space mapping (ISM) is reviewed. The proposed CAD algorithm is discussed and demonstrated through a practical spiral optimization example. The advantages of the algorithm include a reduction in the need for CPU-expensive EM data, and the elimination of the need for defining iteration-dependent constraints and specific format for the objective/constraint functions. The related work has already been published in [37].

2.2 Different Types of Spiral Inductors

Square spiral inductors are popular because of the simplicity of their layout. However, other polygonal spirals have also been used in circuit design. Some designers prefer polygons with more than four sides to improve performance. Among these, hexagonal and octagonal inductors are widely used. Fig. 2.1(a)–(d) shows the layout for square, hexagonal, octagonal, and circular inductors.

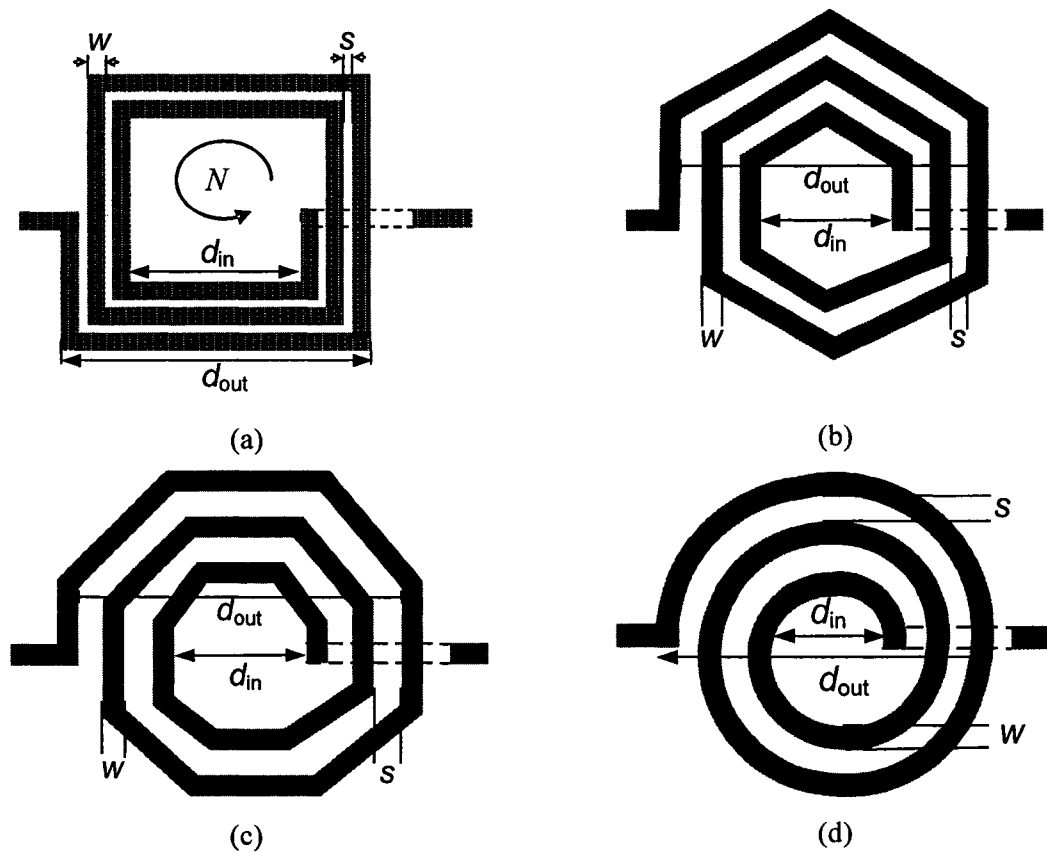


Figure 2.1 On-chip spiral inductor realizations: (a) square, (b) hexagonal, (c) octagonal, and (d) circular.

Cross section of a spiral inductor fabricated in a sample CMOS process is shown in Fig. 2.2. Two metal layers are used; the top layer for the spiral inductor and the lower layer for the underpass (shown by the dotted line in Fig. 2.1). For a given shape, an inductor is completely specified by the number of turns N , the turn width w , the turn spacing s , and any one of the following: the outer diameter d_{out} , the inner diameter d_{in} , the average diameter $d_{avg} = 0.5 \times (d_{out} + d_{in})$, or the fill ratio, defined as $\rho = (d_{out} - d_{in}) / (d_{out} + d_{in})$.

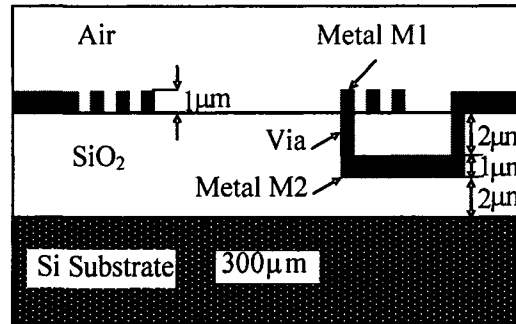


Figure 2.2 Cross-section of a spiral inductor [36].

2.3 Spiral Inductor Circuit Model and Related Formulations

Significant work has been done to model spiral inductors using lumped circuit models [5][6]. Fig. 2.3 illustrates a commonly used model. In this circuit model, the inductor L_s models the inductance of the spiral inductor and the resistor R_s models the resistance of the metal trace. C_s represents the direct coupling through the overlap between the spiral and the underpass. The substrate is modeled by three components. The capacitor C_{ox} models the oxide capacitance between the spiral and the substrate. The capacitor C_{si} and

the resistor R_{si} represent the capacitance and resistance of silicon substrate. The parasitic resistors and capacitors in this model have simple physically intuitive expressions [5][6], using the geometric parameters of the spiral inductor and technology-related parameters of the fabrication process. These equations are:

$$R_s = \frac{l}{\sigma w \delta (1 - e^{-l/\delta})} \quad (2.1)$$

$$C_s = n w^2 \frac{\epsilon_{ox}}{t_{ox M1-M2}} \quad (2.2)$$

$$C_{ox} = \frac{1}{2} l w \frac{\epsilon_{ox}}{t_{ox}} \quad (2.3)$$

$$C_{si} = \frac{1}{2} l w C_{Sub} \quad (2.4)$$

$$R_{si} = \frac{2}{l w G_{Sub}} \quad (2.5)$$

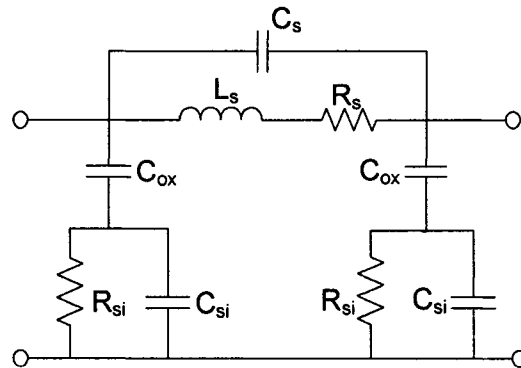


Figure 2.3 Equivalent circuit model of the spiral inductor [5].

where l is the total length of spiral, σ is the metal conductivity at DC, w is the line width, δ is the metal skin depth, t is the metal thickness, n is the number of crossovers between the spiral and the underpass, ϵ_{ox} is the oxide permittivity, $t_{\text{ox M1-M2}}$ is the oxide thickness between the spiral and the underpass, t_{ox} is the oxide thickness between the spiral and the substrate, C_{sub} is the substrate capacitance per unit area and G_{sub} is the substrate conductance per unit area. Since the substrate impedance is difficult to model, C_{sub} and G_{sub} are generally treated as fitting parameters. (Typical value for C_{sub} is 10^{-3} to 10^{-2} fF/ μm^2 and typical value for G_{sub} is 10^{-7} S/ μm^2). The metal skin depth is given by

$$\delta = \sqrt{\frac{1}{\pi f \mu_0 \sigma}} \quad (2.6)$$

where f is the frequency and $\mu_0 = 4\pi \times 10^{-7}$ H/m is the permeability of free space. The inductance value (L_s) in this model lacks a simple but accurate expression. In the following subsection some of the existing inductance expressions are introduced.

2.3.1 Inductance Calculation

Many methods have been proposed to calculate inductance L_s . Some of the more accurate ones based on empirical equations are demonstrated here.

Inductance calculated by modified Wheeler formula (L_{mw}) is proposed in [8]

$$L_{\text{mw}} = K_1 \mu_0 \frac{N^2 d_{\text{avg}}}{1 + K_2 \rho} \quad (2.7)$$

where coefficients K_1 and K_2 are layout dependent and are shown in Table 2.1, μ_0 is the permeability of free space, N is the number of turns, $d_{avg} = 0.5 \times (d_{out} + d_{in})$ is the average diameter, and ρ is the fill-ratio defined as $\rho = (d_{out} - d_{in}) / (d_{out} + d_{in})$. Equation (2.7) is used in section 2.5 for inductance calculation of the coarse model in the space mapping optimization process.

TABLE 2.1 COEFFICIENTS FOR MODIFIED WHEELER EXPRESSION

Layout	K_1	K_2
Square	2.34	2.75
Hexagonal	2.33	3.82
Octagonal	2.25	3.55

In [8] an expression based on current sheet approximations is given.

$$L_{cursh} = \frac{\mu N^2 d_{avg} c_1}{2} [\ln(c_2 / \rho) + c_3 \rho + c_4 \rho^2] \quad (2.8)$$

where the coefficients c_i are layout dependent and are shown in Table 2.2.

TABLE 2.2 COEFFICIENTS FOR CURRENT SHEET EXPRESSION

Layout	c_1	c_2	c_3	c_4
Square	1.27	2.07	0.18	0.13
Hexagonal	1.09	2.23	0.00	0.17
Octagonal	1.07	2.29	0.00	0.19
Circle	1.00	2.46	0.00	0.20

Another formula is the monomial expression proposed in [8]

$$L_{\text{mon}} = \beta d_{\text{out}}^{\alpha_1} w^{\alpha_2} d_{\text{avg}}^{\alpha_3} N^{\alpha_4} s^{\alpha_5} \quad (2.9)$$

where L_{mon} is the inductance in nH, d_{out} is the outer diameter in μm , w is the metal width in μm , d_{avg} is the average diameter in μm , N is the number of turns and s is the turn spacing in μm . The coefficients β and α_i are layout dependent and extracted through data fitting. These coefficients are given in Table 2.3.

TABLE 2.3 COEFFICIENTS FOR DATA-FITTED MONOMIAL EXPRESSION

Layout	β	α_1	α_2	α_3	α_4	α_5
Square	1.62×10^{-3}	-1.21	-0.147	2.40	1.78	-0.030
Hexagonal	1.28×10^{-3}	-1.24	-0.174	2.47	1.77	-0.049
Octagonal	1.33×10^{-3}	-1.21	-0.163	2.43	1.75	-0.049

In [38] it is shown that the inductance can be calculated from the Y -parameters (or Z -parameters) as

$$L = -\frac{1}{2\pi f} \text{Im}\left(\frac{1}{Y_{12}}\right) \quad (2.10)$$

where f is the frequency. Equation (2.10) is used in section 2.5 for inductance calculation of the fine model using Y -parameters obtained from the EM simulations in the space mapping optimization process.

2.3.2 Quality Factor

Typically, the efficiency of any inductor, *e.g.* on-chip spiral inductor, is measured by its Q . The most fundamental definition for Q of the inductor is [39]

$$Q = 2\pi \cdot \frac{\text{energy stored}}{\text{energy loss in one oscillation cycle}}. \quad (2.11)$$

For an inductor, only the energy stored in the magnetic field is of interest. Any energy stored in the inductor's electric field, because of the parasitic capacitances is harmful. Hence as pointed out in [40] Q is proportional to the net magnetic energy stored, *i.e.* difference between the peak magnetic and electric energies.

In [40], a one port equivalent circuit model of an inductor (Fig. 2.4), which is the circuit model of Fig. 2.3 with one end grounded, is used to calculate the quality factor. The frequency-dependent components R_p and C_p are calculated as [40]

$$R_p = \frac{1}{\omega^2 C_{ox}^2 R_{si}} + \frac{R_{si} (C_{ox} + C_{si})^2}{C_{ox}^2} \quad (2.12)$$

$$C_p = C_{ox} \frac{1 + \omega^2 (C_{ox} + C_{si}) C_{si} R_{si}^2}{1 + \omega^2 (C_{ox} + C_{si})^2 R_{si}^2}. \quad (2.13)$$

The energies are expressed as [40]

$$E_{\text{peakelectric}} = \frac{V_0^2 (C_s + C_p)}{2} \quad (2.14)$$

$$E_{\text{peak magnetic}} = \frac{V_0^2 L_s}{2 [(\omega L_s)^2 + R_s^2]} \quad (2.15)$$

$$E_{\text{loss}} = \frac{2\pi}{\omega} \times \frac{V_0^2}{2} \times \left[\frac{1}{R_p} + \frac{R_s}{(\omega L_s)^2 + R_s^2} \right]. \quad (2.16)$$

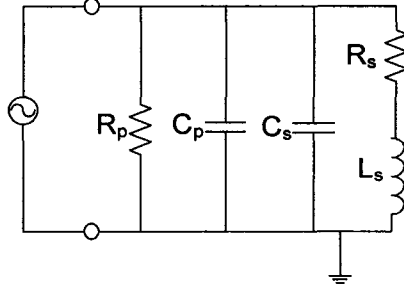


Figure 2.4 Equivalent circuit model of the spiral inductor with one end connected to the ground [40].

According to (2.11) the Q can be calculated as

$$\begin{aligned}
 Q &= 2\pi \times \frac{E_{\text{peak magnetic}} - E_{\text{peak electric}}}{E_{\text{loss}}} \\
 &= \frac{\omega L_s}{R_s} \times \frac{R_p}{R_p + [(\omega L_s / R_s)^2 + 1]R_s} \times \left[1 - \frac{R_s^2(C_s + C_p)}{L_s} - \omega^2 L_s(C_s + C_p) \right]. \quad (2.17)
 \end{aligned}$$

Equation (2.17) is used in section 2.5 for the Q calculation of the coarse model in the space mapping optimization process.

Alternatively Q can also be calculated from the Y parameters (or Z parameters) as [38]

$$Q = -\frac{\text{Im}(Y_{11})}{\text{Re}(Y_{11})}. \quad (2.18)$$

Equation (2.18) is used in section 2.5 for the Q calculation of the fine model using Y -parameters obtained from the EM simulations in the space mapping optimization process.

2.4 Space Mapping Technology

Typically, an engineering design problem involves finding the design parameters (*e.g.*, geometry) which leads to the desired response (*e.g.*, S -parameters). This problem is often solved by an optimization program, which needs to evaluate the response and possible derivatives with regard to design parameters. This information is obtained from a model, *e.g.*, a circuit model or an EM simulator.

Space-mapping (SM) [18] which was introduced by Bandler *et al.* in 1994 has recently emerged as an efficient engine for EM based optimization of passive components. SM is a mathematical tool, which combines the speed of “coarse models” (approximate circuit-based models or empirical models) with the accuracy of “fine models” (CPU-intensive EM solvers) to enable accurate yet fast EM based optimization solutions. SM-based optimization algorithms perform optimization on the coarse model and attempt to tune its response to match that of the fine model. SM has been an active topic of CAD research for over a decade, and several variations of SM such as aggressive space mapping (ASM), [19][20] Implicit space mapping (ISM) [21] and output space mapping (OSM) [22] exist in the RF/microwave literature. In this section, the basic concept of SM and ISM which is used in spiral inductor optimization is reviewed.

2.4.1 Space Mapping (SM) Concept

In Fig. 2.5 [23] \mathbf{x}_c stands for the coarse model design parameters and \mathbf{x}_f stands for the fine model design parameters. \mathbf{R}_c and \mathbf{R}_f represent vectors of responses, *e.g.* $|S_{11}|$ at selected

frequency points, for the coarse and fine models respectively. The original design problem is to find

$$\mathbf{x}_f^* \triangleq \arg \min_{\mathbf{x}_f} U(\mathbf{R}_f(\mathbf{x}_f)) \quad (2.19)$$

where U is a suitable objective function, *e.g.* a minimax objective function with upper and lower specifications, and \mathbf{x}_f^* is the optimal design.

The basic idea of space mapping is to match the coarse model and the fine model during the optimization by finding a mapping P between the fine and coarse model parameter spaces

$$\mathbf{x}_c = P(\mathbf{x}_f) \quad (2.20)$$

such that the response of the fine and coarse model match each other in the region of interest as

$$\mathbf{R}_c(P(\mathbf{x}_f)) \approx \mathbf{R}_f(\mathbf{x}_f). \quad (2.21)$$

Once such a mapping is developed, estimation of \mathbf{x}_f^* can be made without optimization of the fine model by using

$$\mathbf{x}_f^* \triangleq P^{-1}(\mathbf{x}_c^*). \quad (2.22)$$

In (2.22), \mathbf{x}_c^* is the optimal solution in the coarse space.

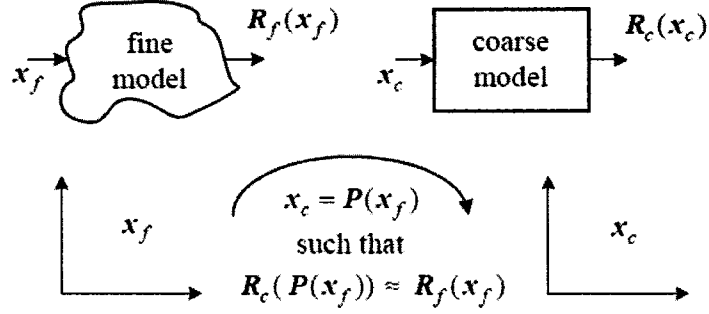


Figure 2.5 Overview of space mapping [23].

2.4.2 Implicit Space Mapping (ISM) [21]

Implicit space mapping (ISM), in what is often referred to as parameter extraction (PE), calibrates certain selected coarse model preassigned parameters, *e.g.* dielectric constant and height of the substrate, to match the response of the coarse and fine models. With these re-calibrated preassigned parameters now fixed in value, the enhanced coarse model (surrogate) is then re-optimized to obtain a new design. This new design is applied to the fine model. These steps are repeated until the design specification is satisfied.

In accordance with [21], let $\mathbf{R}_f(\mathbf{x}_f)$ represent a response vector of the fine model at input \mathbf{x}_f and $\mathbf{R}_c(\mathbf{x}_c, \mathbf{p})$ represent a response vector of the coarse (surrogate) model with \mathbf{x}_c being the design variables and \mathbf{p} being a set of preassigned parameters, which are adjusted by the ISM in order to match the surrogate model with the fine model. $\mathbf{x}_c^{*(i)}$ is defined as the surrogate optimal point at the i^{th} iteration and $\mathbf{x}_c^{*(0)}$ as the initial value. In each i^{th} iteration of PE, the objective is to find

$$\mathbf{p}^{(i)} \triangleq \arg \min_{\mathbf{p}} \left\| \mathbf{R}_f(\mathbf{x}_c^{*(i-1)}) - \mathbf{R}_c(\mathbf{x}_c^{*(i-1)}, \mathbf{p}) \right\| \quad (2.23)$$

Alternatively, the ISM can use multi-point PE, *i.e.* utilize all the fine EM data simulated in the previous iterations as

$$\mathbf{p}^{(i)} \triangleq \arg \min_{\mathbf{p}} \left\| [\mathbf{e}_0^T \mathbf{e}_1^T \dots \mathbf{e}_{i-1}^T]^T \right\| \quad (2.24)$$

where

$$\mathbf{e}_j^T = \mathbf{R}_f(\mathbf{x}_c^{*(j)}) - \mathbf{R}_c(\mathbf{x}_c^{*(j)}, \mathbf{p}), j = 0, \dots, i-1. \quad (2.25)$$

After finding preassigned parameters in the PE step, we optimize the enhanced coarse model (surrogate) to obtain new design parameters by

$$\mathbf{x}_c^{*(i)} \triangleq \arg \min_{\mathbf{x}_c} U(\mathbf{R}_c(\mathbf{x}_c, \mathbf{p}^{(i)})) \quad (2.26)$$

These new design parameters are applied to the fine model. These steps are repeated until the design specification is satisfied. The basic concept of the ISM is illustrated in Fig. 2.6.

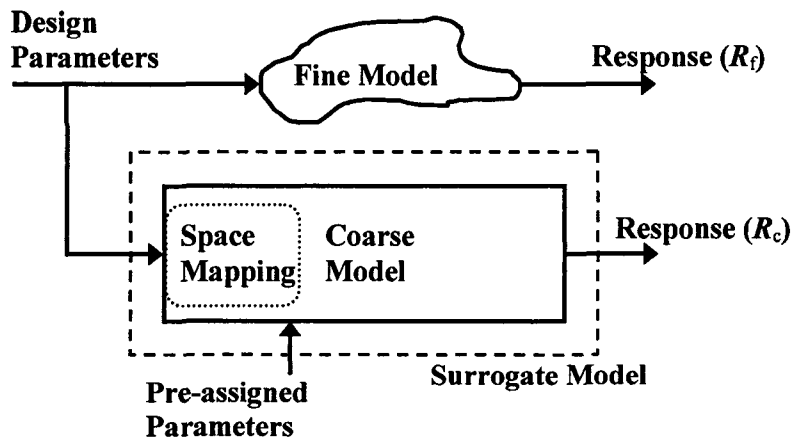


Figure 2.6 Basic concept of the ISM technique [21].

2.5 Proposed SQP Based SM Algorithm for Spiral Inductor

Optimization

In this section, implicit space mapping (ISM) is employed for the optimization of spiral inductors to combine the computational efficiency of the circuit model and the accuracy of the EM simulations. The inductor's circuit model discussed in section 2.3 is used as the coarse model and full-wave EM simulations of the spiral inductor in Ansoft *HFSS* environment are used as the fine data/model.

2.5.1 Parameter Extraction

In this work, PE is performed in two steps. In the first step, calibration of the surrogate model's inductance is carried out. In the second step, calibration of the surrogate's Q is performed. Both inductance L_f and quality factor Q_f of the fine model are calculated by plugging in the simulated Y -parameters from Ansoft *HFSS* into (2.27) and (2.28) respectively.

$$L_f = -\frac{1}{2\pi f} \text{Im}\left(\frac{1}{Y_{12}}\right) \quad (2.27)$$

$$Q_f = -\frac{\text{Im}(Y_{11})}{\text{Re}(Y_{11})} \quad (2.28)$$

Let $\mathbf{x}_c = [d_{\text{out}} \ w \ N \ s]^T$ be the design vector, where d_{out} is the outer length, w is the metal line width, N is the number of turns, and s is the space between metal lines. \mathbf{x}_c is constant

in PE and new parameters (pre-assigned) are defined to match the circuit (surrogate) model response $\mathbf{R}_c = [L_c \ Q_c]^T$, which is defined in the following two steps, to the fine model response $\mathbf{R}_f = [L_f \ Q_f]^T$. Performing PE in two steps has an advantage that in each step there are few preassigned parameters to be evaluated which leads to better convergence in the spiral inductor optimization process.

Step 1) Inductance Calibration: The pre-assigned parameters $\mathbf{p}_1 = [z_1 \ z_2]^T$ and surrogate inductance L_c are defined as

$$L_c = z_1 L_s^{z_2}. \quad (2.29)$$

L_s is the inductor in Fig. 2.3 and the modified Wheeler formula is used to calculate its inductance as

$$L_s = K_1 \mu_0 \frac{N^2 d_{\text{avg}}}{1 + K_2 \rho}. \quad (2.30)$$

It should be noted that L_c is a function of \mathbf{x}_c and \mathbf{p}_1 and that \mathbf{x}_c is constant during the PE step. Parameters \mathbf{p}_1 can be found using

$$\mathbf{p}_1^{(i)} \triangleq \arg \min_{\mathbf{p}_1} \left\| [e_0 \ e_1 \ \dots \ e_{i-1}]^T \right\|, \quad (2.31)$$

where

$$e_j = L_f(\mathbf{x}_c^{*(j)}) - L_c(\mathbf{x}_c^{*(j)}, \mathbf{p}_1), \ j = 0, \dots, i-1. \quad (2.32)$$

Step 2) Quality factor Calibration: The pre-assigned parameters $\mathbf{p}_2 = [y_1 \ \dots \ y_8]^T$ are defined as

$$SMR_s = y_1 R_s^{y_2}, \quad (2.33)$$

$$SMC_s = y_3 C_s^{y_4}, \quad (2.34)$$

$$SMR_p = y_5 R_p^{y_6}, \quad (2.35)$$

$$SMC_p = y_7 C_p^{y_8}. \quad (2.36)$$

The surrogate model's quality factor (Q_c) can be calculated by substituting L_s , R_s , C_s , R_p and C_p in (2.17) with L_c , SMR_s , SMC_s , SMR_p and SMC_p respectively. It should be noted that Q_c is a function of \mathbf{x}_c , \mathbf{p}_1 and \mathbf{p}_2 , and that \mathbf{x}_c is constant and \mathbf{p}_1 is obtained from inductance calibration. Parameters \mathbf{p}_2 can be found using

$$\mathbf{p}_2^{(i)} \triangleq \arg \min_{\mathbf{p}_2} \left\| [e_0 \ e_1 \dots \ e_{i-1}]^T \right\|, \quad (2.37)$$

where

$$e_j = Q_f(\mathbf{x}_c^{*(j)}) - Q_c(\mathbf{x}_c^{*(j)}, \mathbf{p}_1, \mathbf{p}_2), \quad j = 0, \dots, i-1. \quad (2.38)$$

Nonlinear equations (2.31) and (2.37) are solved using the “lsqnonlin” function in MATLAB.

2.5.2 Optimization Objective

The problem here is to find the inductor design parameters $\mathbf{x}_c = [d_{out} \ w \ N \ s]^T$ knowing the pre-assigned parameters \mathbf{p}_1 and \mathbf{p}_2 from the PE step. To this end, the surrogate model's optimization objective is formulated as

$$\begin{aligned}
& \text{maximize} && Q_c(\mathbf{x}_c, \mathbf{p}_1, \mathbf{p}_2) \\
& \text{subject to} && L_{s\min} \leq L_c(\mathbf{x}_c, \mathbf{p}_1) \leq L_{s\max} \\
& && d_{\text{avg}} + Ns + Nw \leq d_{\text{out}} \\
& && (2N + 1)(s + w) \leq d_{\text{out}} \\
& && d_{\text{out min}} \leq d_{\text{out}} \leq d_{\text{out max}} \\
& && w_{\min} \leq w \leq w_{\max} \\
& && s_{\min} \leq s \leq s_{\max} \\
& && N_{\min} \leq N \leq N_{\max}
\end{aligned} \tag{2.39}$$

The geometry/layout of the spiral inductor is optimized with an aim to maximize Q at the desired frequency while obtaining the user-specified inductance. The target inductance is accounted for by the first constraint. The second and the third constraints guarantee that the physical layout is realistic. The remaining constraints denote the lower and upper bounds of the inductor's geometry. In this work, after each iteration, the number of turns N obtained from optimization of (2.39) is rounded to the two nearest positive integer values k and $k \pm 0.5$. Fixing N to each of these two values, one more optimization is done and the better result is chosen. Considering that L and Q are nonlinear functions of the design variables, the proposed SQP based algorithm solves (2.39) using the "fmincon" function in MATLAB. It should be noted that Q_c is multiplied by a negative sign to become an appropriate objective function for "fmincon" since minimizing $-Q_c$ is equivalent to maximizing Q_c . The flow-chart of the proposed algorithm is shown in Fig. 2.7.

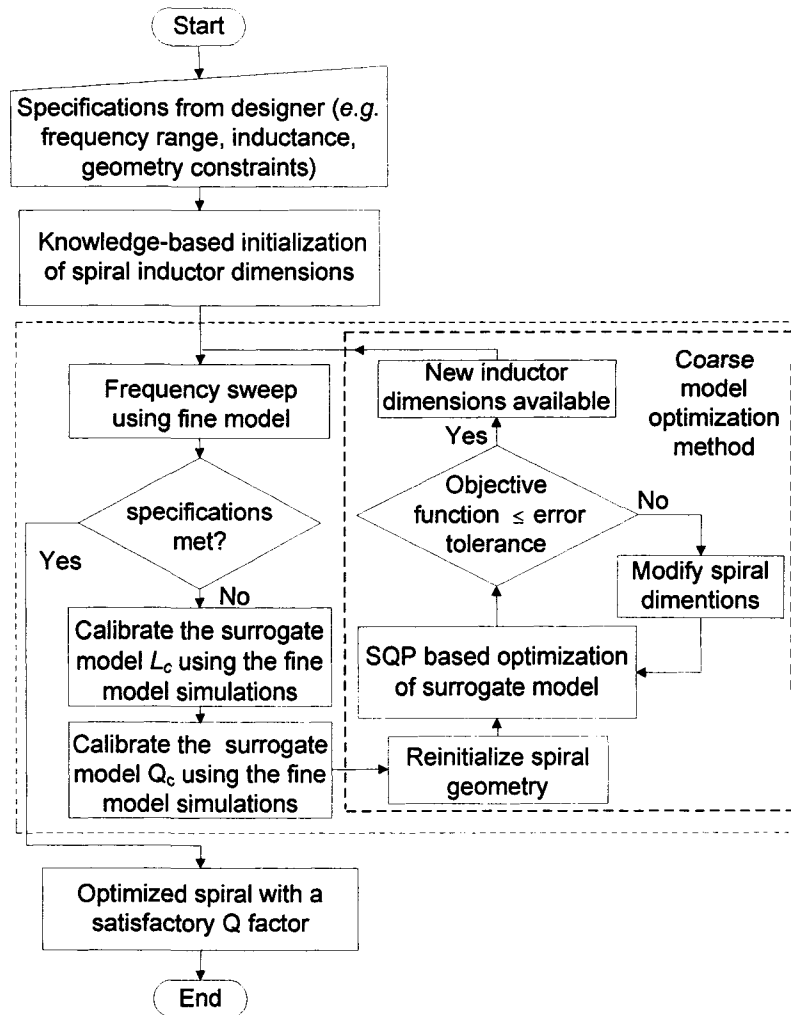


Figure 2.7 Flow-chart of the proposed SQP based space mapping algorithm.

2.6 Example of Spiral Inductor Design/Optimization

In this section, the proposed algorithm is applied to the design/optimization of a spiral inductor built using the sample CMOS process shown in Fig. 2.2. The conductivity of the Si substrate is 5 S/m. Two metal layers of 1 μ m thickness, M_1 and M_2 , are used for the spiral inductor and the underpass. The conductivity of the metal layers is 3×10^7 S/m. The

user-requirement for design/optimization is to achieve the highest Q and a 4 nH inductance at 3 GHz. The tolerance for the inductance is 5%, which means that L_c can lie within the range 3.8-4.2 nH. User-constraints on the design parameters are listed in Table 2.4.

The results of the proposed algorithm are compared and validated with those from a recent SM algorithm based on geometric programming (GP) [36] and from traditional exhaustive enumeration (see Table 2.5). In the case of the proposed SQP based ISM, a satisfactory inductor design emerges after using 5 fine EM simulations, which is just half the number of fine simulations used by the GP based ISM. The L and Q of the spiral inductor (*i.e.* row 3 of Table 2.5) are a result of GP based ISM employing “*HFSS data*” as opposed to GP based ISM [36] that used “*Sonnet EM data*”. In enumeration, the sampling steps in the design region are 5 μm for d_{out} , 1 μm for w , one turn for N and 2 μm for s . Optimization results from the proposed algorithm are close to those from the exhaustive enumeration technique, which typically takes several days to converge.

TABLE 2.4 CONSTRAINTS ON DESIGN PARAMETERS

Parameter	Lower Bound	Upper Bound
d_{out}	150 μm	300 μm
w	1 μm	15 μm
N	2.5	7.5
s	2 μm	10 μm

TABLE 2.5 COMPARISON OF INDUCTOR OPTIMIZATION ALGORITHMS

Optimization Method	Optimized Design ($[d_{out} \ w \ N \ s]^T$ in μm)	Q	L (in nH)	No. of EM Data
Proposed SQP based ISM	$[205 \ 10.2 \ 4.5 \ 2]^T$	4.94	3.8	5
GP based ISM	$[203 \ 10 \ 4.5 \ 2]^T$	4.87	3.76	10
Exhaustive Enumeration	$[205 \ 10 \ 4.5 \ 2]^T$	4.9	3.9	13950

2.7 Summary

In this chapter, an SQP based ISM algorithm has been proposed for design/optimization of the on-chip spiral inductors. Starting with user-specifications (*e.g.* those from an RFIC designer), the proposed algorithm yields a satisfactory EM-validated spiral inductor design using very small amount of EM data. Owing to its unique framework, the algorithm neither requires defining iteration-dependent constraints in the PE step nor involves any assumptions in terms of the format of the objective/constraint functions. Furthermore, parameter extraction step has been performed with few preassigned parameters so that better convergence in the spiral inductor optimization process can be achieved.

Chapter 3

Design of a Compact Composite Low-Pass Filter

3.1 Background and Motivation

In many applications of modern communication systems such as harmonic rejection and spurious signal filtering, planar low-pass filters (LPF) are in demand. These LPFs are desired to have compact size and exhibit sharp cutoff frequency response, high selectivity and wide stopband. These requirements are addressed by considering two different aspects of the design cycle, namely, the design of the circuit schematic and the implementation of the elements within the circuit schematic.

For the schematic design, conventional approaches are applying Butterworth or Chebyshev type filters. These kinds of filters have no attenuation poles, so enhancing the selectivity requires high-order design [41]. Elliptic-function filters have attenuation poles near their passbands, making them very attractive for high-selectivity applications.

However, a high-order design is also required to simultaneously ensure a flat response in the passband and a good out-of-band attenuation [42]. In both cases, a compact planar design is practically difficult to achieve due to the number of components. A good design approach that can be promising in such challenging scenarios is composite LPF design by the image parameter method [24][25]. This design approach is explained and used in this chapter to design a LPF.

In the case of implementation, conventional LPFs use shunt stubs and stepped impedance lines [43] which have narrow stopband, poor cutoff response and relatively large size. Coplanar waveguides can also be used to implement circuit elements [44] but in the frequency range of a few GHz they occupy large area [41]. In this work, spiral inductors and metal-insulator-metal (MIM) capacitors are employed for implementation of lumped elements. Although lumped element circuits containing spiral inductors and MIM capacitors typically exhibit a lower quality factor Q than distributed circuits due to smaller element dimensions and the multilevel fabrication process, they have the advantage of smaller size, lower cost, and wider bandwidth characteristic [45]. These characteristics are especially suitable for monolithic microwave integrated circuits (MMICs) where small size requirements are of prime importance.

Recently, a composite LPF with a 1.5GHz cutoff frequency based on microstrip lines has been presented in [46]. However, this filter has several drawbacks including ripples in the passband and larger size. Further, there is a potential for improving the attenuation slope after the cutoff frequency.

In this chapter, design of composite LPFs by the image parameter method is discussed and a design example is presented. The design is then realized using on-chip spiral inductors and MIM capacitors. The space-mapping based CAD algorithm explained in chapter 2 is exploited in order to rapidly yet accurately design/optimize inductors exhibiting high Q s at filter cutoff frequency. The proposed filter is ultra-compact and suitable for MMIC applications. Full-wave EM simulations indicate a flat passband, sharp cutoff and wide stopband. The related work has been submitted in [47].

3.2 Composite Filter Design by the Image Parameter Method

[24][25]

There are two methods available to synthesize passive filters. One of them is known as the image parameter method and the other as the insertion loss method. The image parameter method involves the specification of passband and stopband characteristic for a cascade of two-port networks. The method is relatively simple but has the disadvantage that the filter frequency response cannot be shaped. On the other hand the insertion loss method has the advantage that it can provide a specified filter response. Nevertheless, the image parameter method is useful for LPFs and HPFs. It also finds application in solid-state traveling-wave amplifier design.

3.2.1 Image Impedances and Transfer Functions for Two-Port Networks

For the analysis and design of filters by the image parameter method, the first requirement is to define the image impedances and voltage transfer function for an arbitrary reciprocal two-port network.

Fig.3.1 shows a two-port network with its $ABCD$ parameters. The current at port 2 has the direction according to the convention for $ABCD$ parameters. The image impedances, Z_{i1} and Z_{i2} , for this network are defined as

Z_{i1} = input impedance at port 1 when port 2 is terminated with Z_{i2} ,

Z_{i2} = input impedance at port 2 when port 1 is terminated with Z_{i1} .

It can be observed that terminating the ports in their image impedances causes them to be matched. Expressions for the image impedances in terms of the $ABCD$ parameters of a network can be derived through the following procedure.

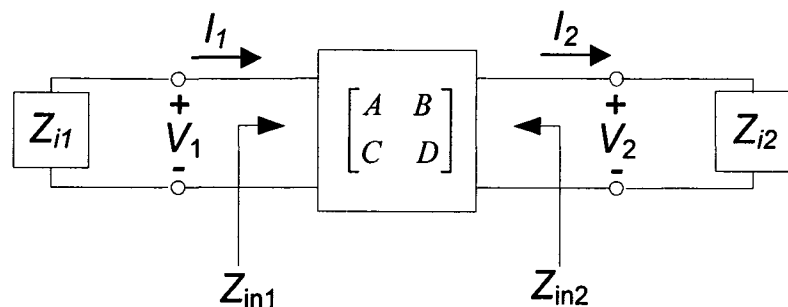


Figure 3.1 A two-port network terminated in its image impedances.

Voltages and currents of the ports are related as

$$V_1 = AV_2 + BI_2, \quad (3.1a)$$

$$I_1 = CV_2 + DI_2. \quad (3.1b)$$

The input impedance at port 1, with port 2 terminated in Z_{i2} such that $V_2 = Z_{i2}I_2$, is

$$Z_{in1} = \frac{V_1}{I_1} = \frac{AV_2 + BI_2}{CV_2 + DI_2} = \frac{AZ_{i2} + B}{CZ_{i2} + D}. \quad (3.2)$$

Equation (3.1) is solved for V_2 and I_2 by inverting the $ABCD$ matrix. Since $AD - BC = 1$ for a reciprocal network, it is obtained

$$V_2 = DV_1 - BI_1, \quad (3.3a)$$

$$I_2 = -CV_1 + AI_1. \quad (3.3b)$$

Then the input impedance at port 2, with port 1 terminated in Z_{i1} such that $V_1 = -Z_{i1}I_1$, can be found as

$$Z_{in2} = \frac{-V_2}{I_2} = -\frac{DV_1 - BI_1}{-CV_1 + AI_1} = \frac{DZ_{i1} + B}{CZ_{i1} + A}. \quad (3.4)$$

It is desired that $Z_{in1} = Z_{i1}$ and $Z_{in2} = Z_{i2}$, so (3.2) and (3.4) give two equations for the image impedances:

$$Z_{i1}(CZ_{i2} + D) = AZ_{i2} + B, \quad (3.5a)$$

$$Z_{i2}(CZ_{i1} + A) = DZ_{i1} + B. \quad (3.5b)$$

Z_{i1} and Z_{i2} are solved to be

$$Z_{i1} = \sqrt{\frac{AB}{CD}}, \quad (3.6a)$$

$$Z_{i2} = \sqrt{\frac{BD}{AC}}, \quad (3.6b)$$

with $Z_{i2} = DZ_{i1}/A$. For the symmetric network $A = D$ and $Z_{i1} = Z_{i2}$ as expected.

Now the voltage transfer function for a two-port network terminated in its image impedances is studied. The output voltage at port 2 of Fig. 3.2 considering (3.3a) is

$$V_2 = DV_1 - BI_1 = \left(D - \frac{B}{Z_{i1}} \right) V_1 \quad (3.7)$$

since now $V_1 = I_1 Z_{i1}$ so the voltage ratio is

$$\frac{V_2}{V_1} = D - \frac{B}{Z_{i1}} = D - B \sqrt{\frac{CD}{AB}} = \sqrt{\frac{D}{A}} (\sqrt{AD} - \sqrt{BC}). \quad (3.8a)$$

The current ratio can be expressed similarly as

$$\frac{I_2}{I_1} = -C \frac{V_1}{I_1} + A = -CZ_{i1} + A = \sqrt{\frac{A}{D}} (\sqrt{AD} - \sqrt{BC}). \quad (3.8b)$$

The propagation factor for the network can be defined as

$$e^{-\gamma} = \sqrt{AD} - \sqrt{BC}, \quad (3.9)$$

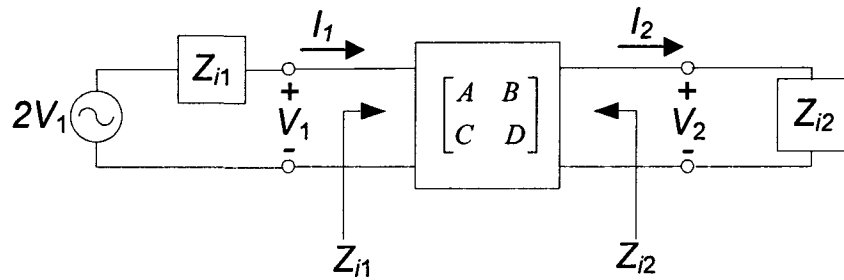


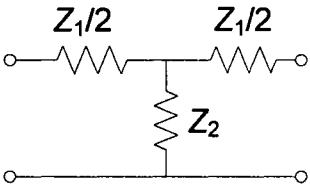
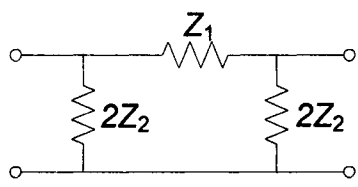
Figure 3.2 A two-port network terminated in its image impedances and driven with a voltage generator.

with $\gamma = \alpha + j\beta$. Since $e^\gamma = 1/(\sqrt{AD} - \sqrt{BC}) = (AD - BC)/(\sqrt{AD} - \sqrt{BC}) = \sqrt{AD} + \sqrt{BC}$, and $\cosh \gamma = (e^\gamma + e^{-\gamma})/2$, so

$$\cosh \gamma = \sqrt{AD}. \quad (3.10)$$

T and π circuits are two types of common two-port networks, which can be expressed in symmetric form. Table 3.1 lists some important parameters, most notably the image impedances and propagation factors, for these two networks.

TABLE 3.1 IMAGE PARAMETERS FOR T AND π NETWORKS [25]

 <p style="text-align: center;">T Network</p>	 <p style="text-align: center;">π Network</p>
<p><i>ABCD</i> parameters:</p> $A = 1 + Z_1/2Z_2$ $B = Z_1 + Z_1^2/4Z_2$ $C = 1/Z_2$ $D = 1 + Z_1/2Z_2$	<p><i>ABCD</i> parameters:</p> $A = 1 + Z_1/2Z_2$ $B = Z_1$ $C = 1/Z_2 + Z_1/4Z_2^2$ $D = 1 + Z_1/2Z_2$
<p><i>Z</i> parameters:</p> $Z_{11} = Z_{22} = Z_2 + Z_1/2$ $Z_{12} = Z_{21} = Z_2$	<p><i>Y</i> parameters:</p> $Y_{11} = Y_{22} = 1/Z_1 + 1/2Z_2$ $Y_{12} = Y_{21} = 1/Z_1$
<p>Image impedance:</p> $Z_{iT} = \sqrt{Z_1 Z_2} \sqrt{1 + Z_1/4Z_2}$	<p>Image impedance:</p> $Z_{i\pi} = \sqrt{Z_1 Z_2} / \sqrt{1 + Z_1/4Z_2} = Z_1 Z_2 / Z_{iT}$
<p>Propagation constant:</p> $e^\gamma = 1 + Z_1/2Z_2 + \sqrt{Z_1/Z_2 + Z_1^2/4Z_2^2}$	<p>Propagation constant:</p> $e^\gamma = 1 + Z_1/2Z_2 + \sqrt{Z_1/Z_2 + Z_1^2/4Z_2^2}$

3.2.2 Constant- k Filter Sections

The constant- k section by itself can be used to design either a low-pass or a high-pass filter. Fig. 3.3 shows T and π form networks which are low-pass filters. In this subsection T networks and π networks are studied respectively.

Comparing the T network with the relations given in Table 3.1, $Z_1 = j\omega L$ and $Z_2 = 1/j\omega C$, so the image impedance is

$$Z_{iT} = \sqrt{\frac{L}{C}} \sqrt{1 - \frac{\omega^2 LC}{4}}. \quad (3.11)$$

A cutoff frequency, ω_c , and a nominal characteristic impedance, R_0 , are defined respectively as

$$\omega_c = \frac{2}{\sqrt{LC}}, \quad (3.12)$$

$$R_0 = \sqrt{\frac{L}{C}} = k, \quad (3.13)$$

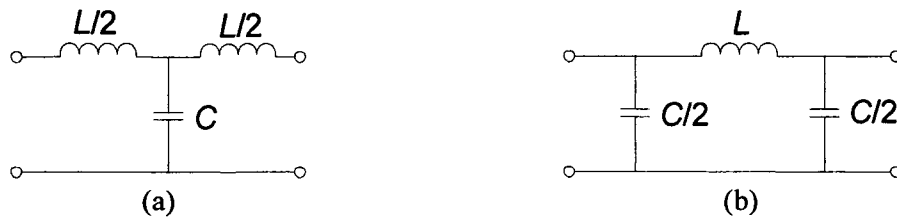


Figure 3.3 Low-pass constant- k filter sections in T and π form. (a) T -section.
(b) π -section.

where k is a constant, (3.11) can then be rewritten as

$$Z_{iT} = R_0 \sqrt{1 - \frac{\omega^2}{\omega_c^2}}. \quad (3.14)$$

Based on (3.14) when $\omega = 0$, $Z_{iT} = R_0$.

The propagation factor, also from Table 3.1, is

$$e^\gamma = 1 - \frac{2\omega^2}{\omega_c^2} + \frac{2\omega}{\omega_c} \sqrt{\frac{\omega^2}{\omega_c^2} - 1}. \quad (3.15)$$

For $\omega < \omega_c$, equation (3.14) shows that Z_{iT} is real and (3.15) shows that γ is imaginary, since $\omega^2 / \omega_c^2 - 1$ is negative and $|e^\gamma| = 1$:

$$|e^\gamma|^2 = \left(1 - \frac{2\omega^2}{\omega_c^2}\right)^2 + \frac{4\omega^2}{\omega_c^2} \left(1 - \frac{\omega^2}{\omega_c^2}\right) = 1.$$

Therefore, $\omega < \omega_c$ is the passband of the filter section.

For $\omega > \omega_c$, Equation (3.14) shows that Z_{iT} is imaginary, and (3.15) shows that e^γ is real and $-1 < e^\gamma < 0$ (as seen from the limits as $\omega \rightarrow \omega_c$ and $\omega \rightarrow \infty$). Therefore, $\omega > \omega_c$ is the stopband of the filter section.

Fig. 3.4 shows typical phase and attenuation constants. Near the cutoff frequency attenuation, α , is zero or close to zero, although $\alpha \rightarrow \infty$ as $\omega \rightarrow \infty$. This type of filter is known as a *constant-k* low-pass prototype. There are only two degree of freedom for design (L and C), which can both be expressed in terms of ω_c , the cutoff frequency, and R_0 , the image impedance at zero frequency.

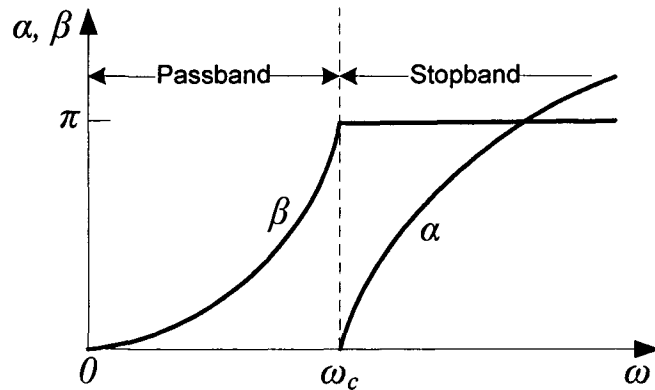


Figure 3.4 Typical passband and stopband characteristic of the low-pass constant- k sections of Fig. 3.3.

The major drawback of this design is that the above results are valid only when the filter section is terminated in its image impedance at both ports. It is to be noted that the image impedance is a function of frequency which is not likely to match a given source or load impedance. To overcome this disadvantage, as well as the low attenuation near cutoff, modified m -derived sections are designed in the following subsection.

In terms of the low-pass π network of fig. 3.3, $Z_1 = j\omega L$ and $Z_2 = 1/j\omega C$, so the propagation factor, the cutoff frequency, ω_c , and nominal characteristic impedance, R_0 , are the same as for the low-pass T network. At $\omega = 0$, $Z_{iT} = Z_{i\pi} = R_0$, where $Z_{i\pi}$ is the image impedance of the low-pass π -network, but Z_{iT} and $Z_{i\pi}$ are generally not equal at other frequencies.

3.2.3 *m*-derived Filter Sections

To overcome the two problems of the constant-*k* filter section namely, relatively slow attenuation rate after cutoff and a nonconstant image impedance, the *m*-derived filter section is designed. The *m*-derived filter section is a modification of the constant-*k* section. The impedances Z_1 and Z_2 in a constant-*k* *T*-section are first replaced with Z'_1 and Z'_2 as shown in Fig. 3.5 (a),(b) where

$$Z'_1 = mZ_1. \quad (3.16)$$

Z'_2 is chosen so that the same value of Z_{iT} as for the constant-*k* section can be achieved.

Thus, from Table 3.1,

$$Z_{iT} = \sqrt{Z_1 Z_2 + \frac{Z_1^2}{4}} = \sqrt{Z'_1 Z'_2 + \frac{Z_1'^2}{4}} = \sqrt{mZ_1 Z'_2 + \frac{m^2 Z_1^2}{4}}. \quad (3.17)$$

Z'_2 is solved to be

$$Z'_2 = \frac{Z_2}{m} + \frac{Z_1}{4m} - \frac{mZ_1}{4} = \frac{Z_2}{m} + \frac{(1-m^2)}{4m} Z_1. \quad (3.18)$$

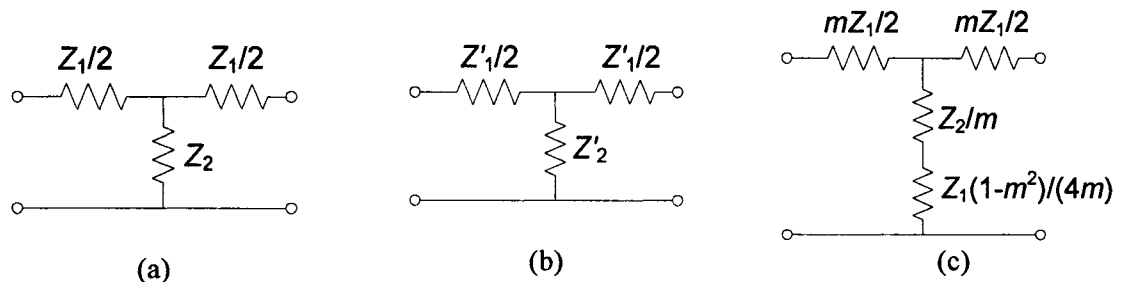


Figure 3.5 Development of an *m*-derived filter section from a constant-*k* section.

(a) Constant-*k* section. (b) General *m*-derived section. (c) Final *m*-derived section.

Since Z_1 and Z_2 represent reactive elements, Z'_2 represents two elements in series, as shown in Fig. 3.5 (c). Note that $m = 1$ reduces to the original constant- k section.

For a low-pass filter, $Z_1 = j\omega L$ and $Z_2 = 1/j\omega C$. Using (3.16) and (3.18) give

$$Z'_1 = j\omega Lm, \quad (3.19a)$$

$$Z'_2 = \frac{1}{j\omega Cm} + \frac{(1-m^2)}{4m} j\omega L, \quad (3.19b)$$

which leads to the circuit of Fig. 3.6. From Table 3.1, the propagation factor is

$$e^\gamma = 1 + \frac{Z'_1}{2Z'_2} + \sqrt{\frac{Z'_1}{Z'_2} \left(1 + \frac{Z'_1}{4Z'_2} \right)}. \quad (3.20)$$

For the low-pass m -derived filter,

$$\frac{Z'_1}{Z'_2} = \frac{j\omega Lm}{(1/j\omega Cm) + j\omega L(1-m^2)/4m} = \frac{-(2\omega m/\omega_c)^2}{1 - (1-m^2)(\omega/\omega_c)^2},$$

where $\omega_c = 2/\sqrt{LC}$ as before. Then,

$$1 + \frac{Z'_1}{4Z'_2} = \frac{1 - (\omega/\omega_c)^2}{1 - (1-m^2)(\omega/\omega_c)^2}.$$

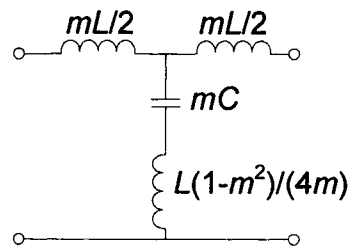


Figure 3.6 Low-pass m -derived T filter section

These results show that for $0 < m < 1$ and for $\omega > \omega_c$, as for the case of the constant- k section, e^γ is real and $|e^\gamma| > 1$. Therefore the stopband begins at $\omega = \omega_c$. However, when $\omega = \omega_\infty$, where

$$\omega_\infty = \frac{\omega_c}{\sqrt{1-m^2}}, \quad (3.21)$$

e^γ approaches infinity, implying ω_∞ corresponds to an attenuation pole. It should be noted that ω_∞ is the resonant frequency of the series LC resonator, thus the attenuation pole can be attributed to this resonator. From (3.21), the location of the attenuation pole can be controlled by appropriately selecting the value of m . By placing the pole close to the cutoff frequency, a very sharp cutoff response can be achieved. A problem with the m -derived section is that, as illustrated in Fig. 3.7, as ω is increased beyond the attenuation pole, the attenuation decreases. Ideally the filter should have infinite attenuation as $\omega \rightarrow \infty$. To this end, the m -derived section can be cascaded with a constant- k section to give the composite attenuation response of Fig. 3.7.

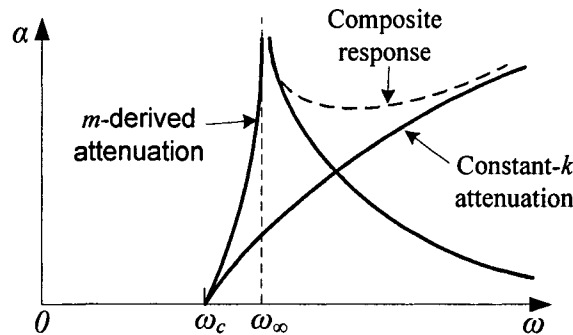


Figure 3.7 Typical attenuation responses for constant- k , m -derived, and composite filters.

The problem of nonconstant image impedance is still remained because the m -derived T -section was designed so that its image impedance was identical to that of the constant- k section (independent of m). However the π -equivalent has the image impedance which depends on m , and it can be used to design an optimum matching section.

Fig. 3.8 shows the development of an m -derived π -section by considering it as a piece of an infinite cascade of m -derived T -sections. Using table 3.1 and (3.14), the image impedance of this network is

$$Z_{i\pi} = \frac{Z'_1 Z'_2}{Z_{iT}} = \frac{Z_1 Z_2 + Z_1^2 (1 - m^2) / 4}{R_0 \sqrt{1 - (\omega / \omega_c)^2}}. \quad (3.22)$$

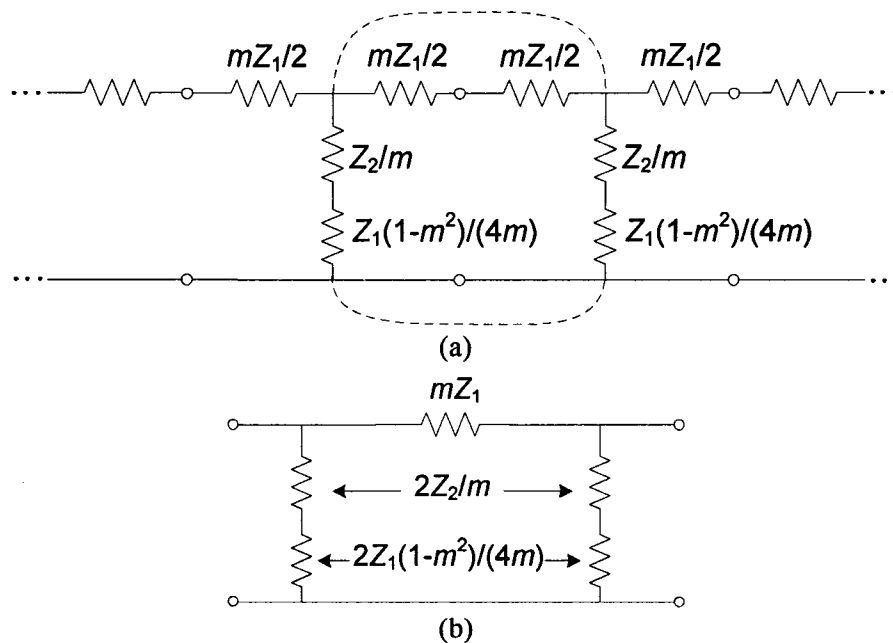


Figure 3.8 Development of an m -derived π -section. (a) Infinite cascade of m -derived T -sections. (b) A de-embedded π -equivalent.

Now $Z_1 Z_2 = L/C = R_0^2$ and $Z_1^2 = -\omega^2 L^2 = -4 R_0^2 (\omega / \omega_c)^2$, so (3.22) reduces to

$$Z_{i\pi} = \frac{1 - (1 - m^2)(\omega / \omega_c)^2}{\sqrt{1 - (\omega / \omega_c)^2}} R_0. \quad (3.23)$$

$Z_{i\pi}$ is a function of m so its variation over the passband of the filter can be minimized by choosing a proper m . For several values of m , variation of $Z_{i\pi}$ with frequency is shown in Fig. 3.9. The best results usually is achieved by $m = 0.6$.

By using the m -derived π -sections at the input and output of the filter, the impedance can be maintained relatively constant with frequency at a value of R_0 . This ensures good matching behavior across the passband of the filter. However, the image impedance of the constant- k and m -derived T -sections, Z_{iT} , does not match $Z_{i\pi}$. A possible solution to this problem is to bisect the π -sections as shown in Fig.3.10. The image impedances of this circuit are $Z_{i1} = Z_{iT}$ and $Z_{i2} = Z_{i\pi}$, which can be shown by finding its $ABCD$ parameters:

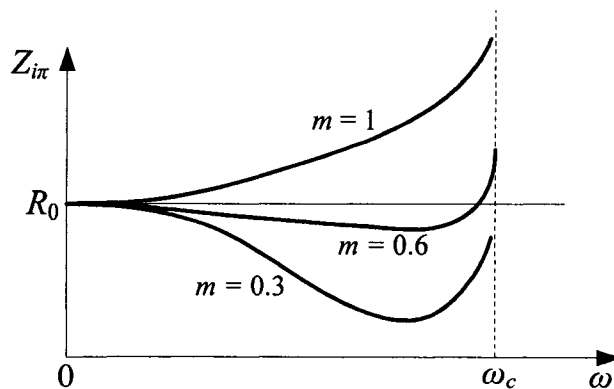


Figure 3.9 Variation of $Z_{i\pi}$ in the passband of a low-pass m -derived section for different values of m .

$$A = 1 + \frac{Z'_1}{4Z'_2}, \quad (3.24a)$$

$$B = \frac{Z'_1}{2}, \quad (3.24b)$$

$$C = \frac{1}{2Z'_2}, \quad (3.24c)$$

$$D = 1, \quad (3.24d)$$

and using (3.6):

$$Z_{i1} = \sqrt{Z'_1 Z'_2 + \frac{Z'^2_1}{4}} = Z_{iT}, \quad (3.25a)$$

$$Z_{i2} = \sqrt{\frac{Z'_1 Z'_2}{1 + Z'_1 / 4Z'_2}} = \frac{Z'_1 Z'_2}{Z_{iT}} = Z_{i\pi}, \quad (3.25b)$$

where (3.17) has been used for Z_{iT} .

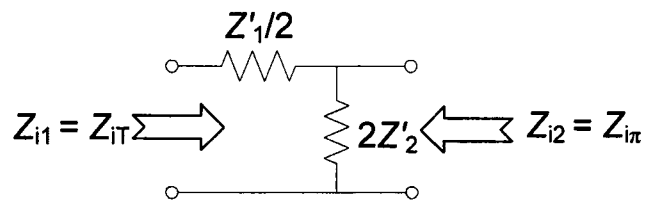


Figure 3.10 A bisected π -section used to match $Z_{i\pi}$ to Z_{iT} .

3.2.4 Composite Filters

By cascading four sections namely, a constant- k , an m -derived sharp cutoff, and two m -derived matching sections a filter of lower order and lower size with desired attenuation and matching properties can be achieved. This type of design is called a composite filter.

The design concept and schematic of a composite LPF is depicted in Fig. 3.11. Design equations are summarized in Table 3.2.

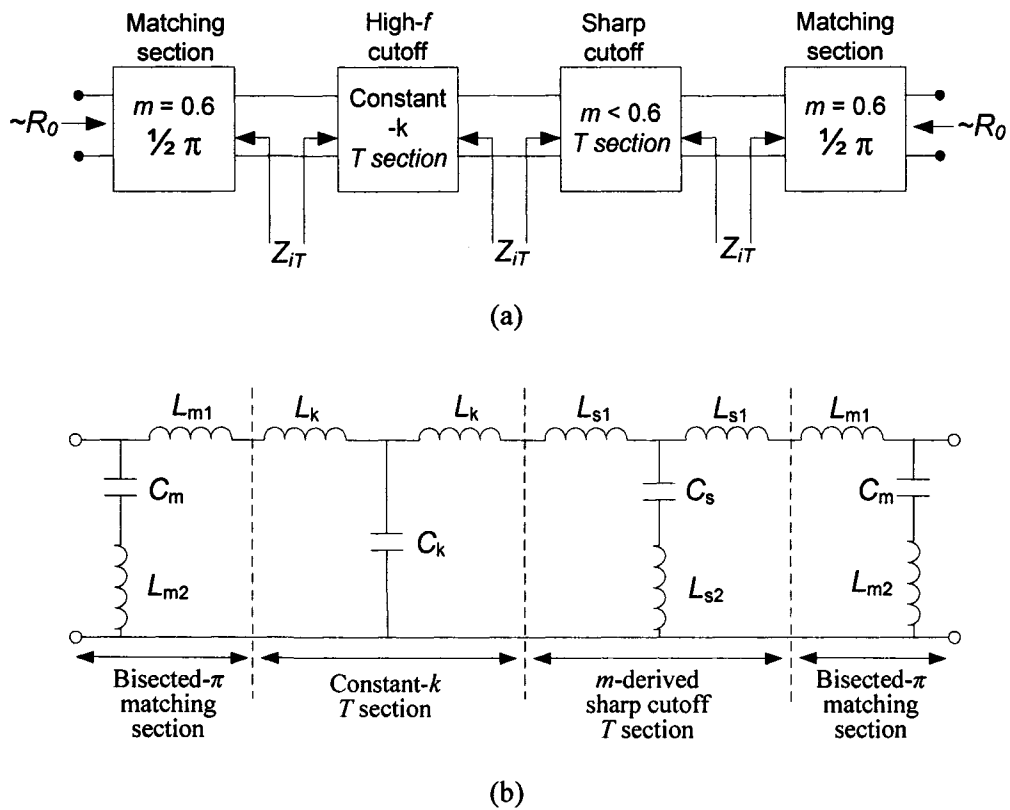


Figure 3.11 (a) Design concept and (b) schematic of a composite LPF.

The sharp-cutoff section, with $m < 0.6$, places an attenuation pole near the cutoff frequency to provide a sharp attenuation response. The constant- k section provides high attenuation further into the stopband. The bisected- π sections at the ends of the filter match the nominal source and load impedances, R_0 , to the internal image impedances, Z_{iT} , of the constant- k and m -derived sections.

3.2.5 A Composite LPF Design Example

The design starts with the calculation of the constant- k section and the m -derived T section with respect to the desired characteristic impedance R_0 , cutoff frequency f_c and the parameter m of the T section. As mentioned earlier, the parameter m sets the placement of an attenuation pole near f_c and obtained by

$$m = \sqrt{1 - (\omega_c / \omega_\infty)^2}. \quad (3.26)$$

The characteristic impedance R_0 has been fixed to 50 Ω in all cases. The required cutoff frequency of the design is 2.8GHz. In our design procedure, different values of m for the T section were evaluated, leading to the final choice of $m = 0.3$ resulting in a good response. Following this, the matching π sections are designed, with their corresponding parameter m set to 0.6 for minimizing the image impedance variation with frequency at the input and output ports. The theoretical expressions and values of the lumped elements are summarized in Table 3.2. Fig. 3.12(a) shows the final composite LPF design obtained after combining the series pairs of inductors in the circuit of Fig. 3.11(b) and optimizing the lumped element values in Agilent *ADS*. The response of this circuit is shown in Fig.

3.12(b). It can be observed that cutoff frequency occurs at 2.8GHz, the first pole, due to $m = 0.3$, occurs at 3GHz and the second pole, due to $m = 0.6$, occurs at 3.55GHz.

TABLE 3.2 THEORETICAL EXPRESSIONS AND VALUES OF THE LUMPED ELEMENTS
($f_c = 2.8$ GHz and $R_0 = 50 \Omega$)

Section	Lumped element	Expression	Value
	L	$2R_0/(2\pi f_c)$	5.684 nH
	C	$2/(R_0 \cdot 2\pi f_c)$	2.274 pF
Constant-k	L_k	$L/2$	2.842 nH
T section	C_k	C	2.274 pF
m-derived sharp	L_{s1}	$mL/2$	0.853 nH
cutoff ($m = 0.3$)	L_{s2}	$L(1-m^2)/(4m)$	4.310 nH
T section	C_s	mC	0.682 pF
m-derived matching	L_{m1}	$mL/2$	1.705 nH
($m = 0.6$)	L_{m2}	$L(1-m^2)/(2m)$	3.031 nH
Bisected-π section	C_m	$mC/2$	0.682 pF

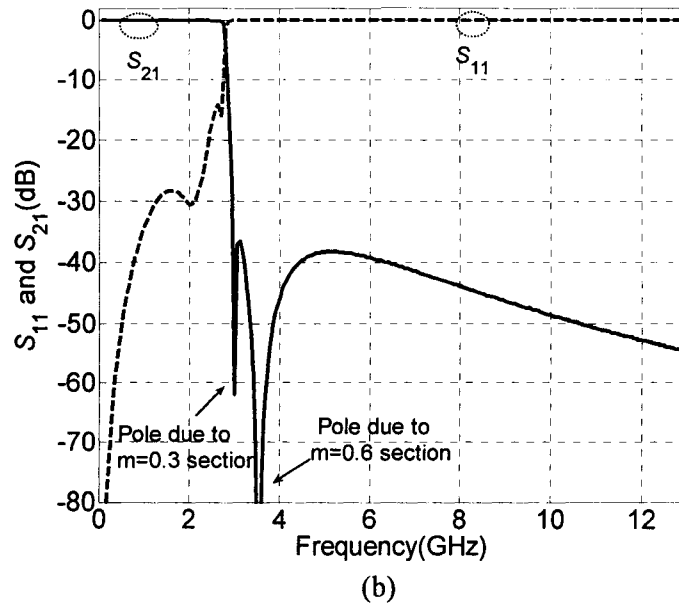
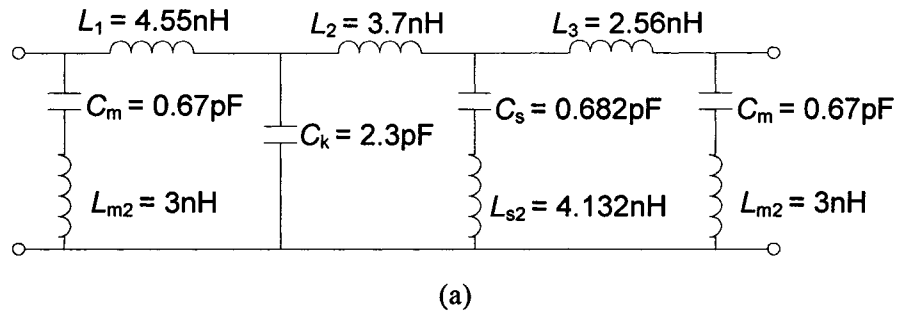


Figure 3.12 (a) Lumped equivalent circuit representation of the composite LPF. (b) The corresponding S -parameter responses.

3.3 Compact Realization of the Designed LPF and Full Wave Simulation Results

The next step is to realize the filter schematic in Fig. 3.12(a), in particular, the inductors and the capacitors. Here, we employ rectangular spiral inductors and MIM capacitors toward realizing a compact composite LPF. Spiral inductors and MIM capacitors possess relatively lower Q s compared to their distributed counterparts due to both smaller dimensions and multi-level fabrication processes. However, they offer certain other advantages such as lower cost and wider bandwidth [45]. These characteristics are especially suitable for MMICs where small size requirements are of prime importance. At frequencies below C-band, MMICs using lumped inductors and capacitors are an order of magnitude smaller than ICs using distributed elements fabricated in microstrip or coplanar waveguide (CPW) [45]. The following steps describe our composite LPF realization.

3.3.1 Choice of Substrate and Metal Layers

A 300 μm silicon substrate with $\epsilon_r = 11.9$ and a 5 μm silicon dioxide with $\epsilon_r = 4$ are employed as the substrate and the oxide layers respectively. Two copper metal layers M_1 and M_2 of 1 μm thickness and 5.8×10^7 S/m conductivity are used for the spiral inductor and the underpass respectively. These metal layers are also used for the MIM capacitor plates. The cross-sections and top views of spiral inductors and MIM capacitors are depicted in Fig. 3.13 and Fig 3.14 respectively.

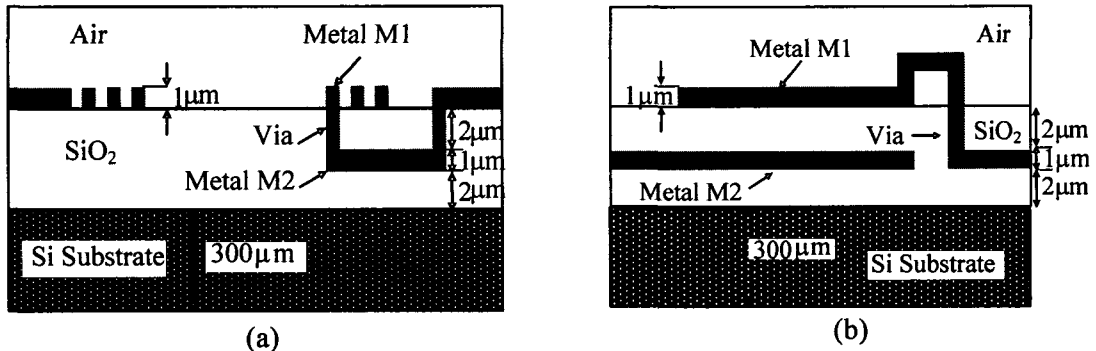


Figure 3.13 Cross-section of (a) spiral inductor and (b) MIM capacitor.

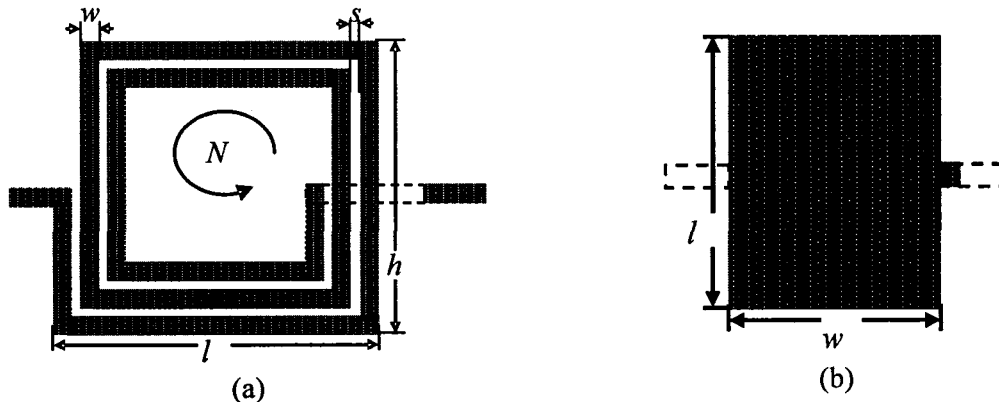


Figure 3.14 Top view of (a) spiral inductor and (b) MIM capacitor.

3.3.2 Design/Optimization of Inductors and Capacitors

The objective of this step is to separately design/realize each of the six inductors and four capacitors with specific values at 2.8 GHz as indicated in Fig. 3.12(a).

As mentioned in chapter 2, at GHz frequencies several phenomena (eddy current, self resonance, *etc.*) affect inductor performance both in terms of its value and Q . As such, accurate design of inductors considering such phenomena demands the use of CPU-

expensive EM simulations. The SQP based space-mapping algorithm proposed in chapter 2 is applied for the design/optimization of all six inductors of Fig. 3.12(a). Starting with desired frequency range and inductance the algorithm leads to spiral inductor designs with high Q s, using minimal amounts of EM data. Considering one inductor at a time, the algorithm first improves the inductor's circuit model, until the circuit model response matches with the EM simulated response of Zeland *IE3D*. This is accomplished by iteratively adjusting what are known as pre-assigned parameters. The next step is to optimize the resulting improved circuit model leading to the specified inductance value at 2.8 GHz. This is achieved by iteratively adjusting the spiral inductor geometry (since the circuit model parameters relate to the inductor geometry). The algorithm leads to a spiral inductor layout offering the desired inductance and an optimal Q . In this work, Q s of all six spiral inductors are in the [8.1, 9] range. It is ensured that the self-resonance frequency of each inductor is much higher than 2.8 GHz.

The four MIM capacitors are initially designed using

$$C = \epsilon_0 \epsilon_r \frac{wl}{d}, \quad (3.27)$$

where ϵ_0 is the free-space permittivity, ϵ_r is the relative dielectric constant (in this work $\epsilon_r = 4$), w and l are the width and length of the parallel plates, and d is the oxide thickness between the two plates (in this work $d = 2 \mu\text{m}$). Next the initial designs are optimized in Zeland *IE3D* leading to specified capacitances at 2.8 GHz.

3.3.3 Design/Optimization of Resonators

In order to connect all the circuit elements, extra transmission lines are needed in the shunt arms of the circuit. These lines affect the inductance and capacitance values. As a result, the dimensions of inductors/capacitors need to be fine-tuned in Zeland *IE3D* to account for the extra lines. The fine tuning for series *LC* resonators in the shunt arms of the filter is done to ensure operation at the desired resonant frequencies. For instance, Fig. 3.15(a) shows one of the three *LC* resonators representing L_{s2} and C_s of Fig. 3.12(a), which is expected to provide the first pole of the composite LPF at 3 GHz. Zeland *IE3D* simulation after fine tuning shows resonance at an acceptable 2.99 GHz. (see Fig. 3.15(b))

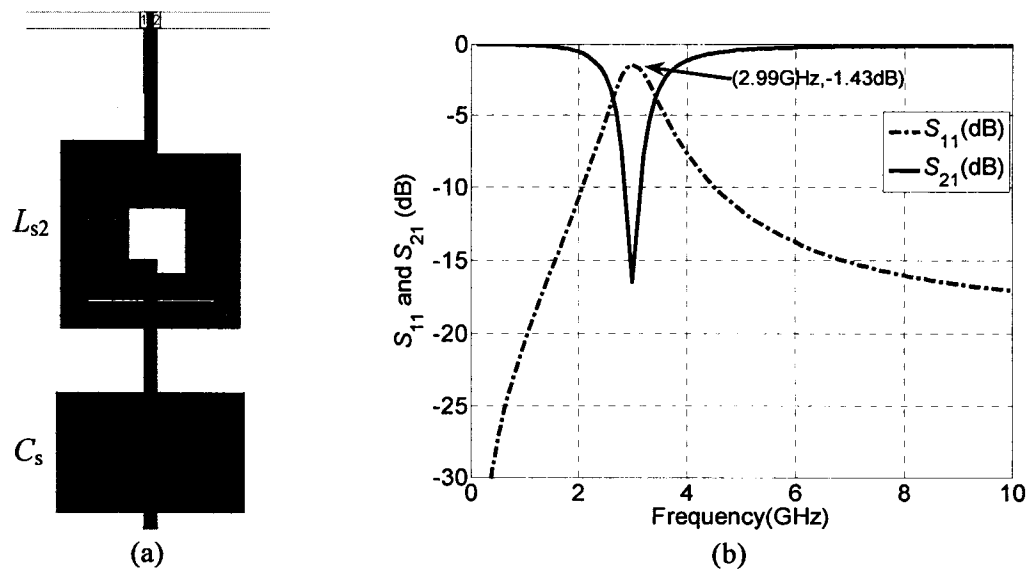


Figure 3.15 (a) A series LC resonator and (b) corresponding EM simulations.

3.3.4 Simulation Results of the Composite LPF

Finally, all the previously discussed sections are combined to build the complete composite LPF, whose layout is shown in Fig. 3.16. Physical dimensions of inductors/capacitors in the final LPF are tabulated in Table 3.3 and 3.4 respectively. For comparison, ideal *ADS* simulations and actual Zeland *IE3D* simulations are presented in Fig. 3.17. EM simulations show a flat response with no ripple, good matching properties, rejection of the attenuated pole as high as 59.5 dB, and low insertion loss in the passband (-0.76 dB at 0.19 GHz). The cutoff frequency is 2.6 GHz and the stopband attenuation is greater than 20 dB over a 12 GHz bandwidth. The slope of S_{21} between cutoff frequency and the first pole is 50 dB/GHz, which is much higher than the 25 dB/GHz slope of the LPF reported in [46]. The proposed filter occupies a compact area of 1.4 mm \times 0.8 mm, which is much smaller than 67 mm \times 23 mm occupied by the LPF in [46]. As shown in Table 3.5, there is a reasonable agreement between the performance of the proposed filter and that of its ideal counterpart. Minor discrepancies are due to both parasitic effects and losses in the spiral inductors and MIM capacitors, which are not considered by the ideal model. The differences between full-wave and ideal model simulations are more significant at higher frequencies because EM effects are stronger in these frequencies.

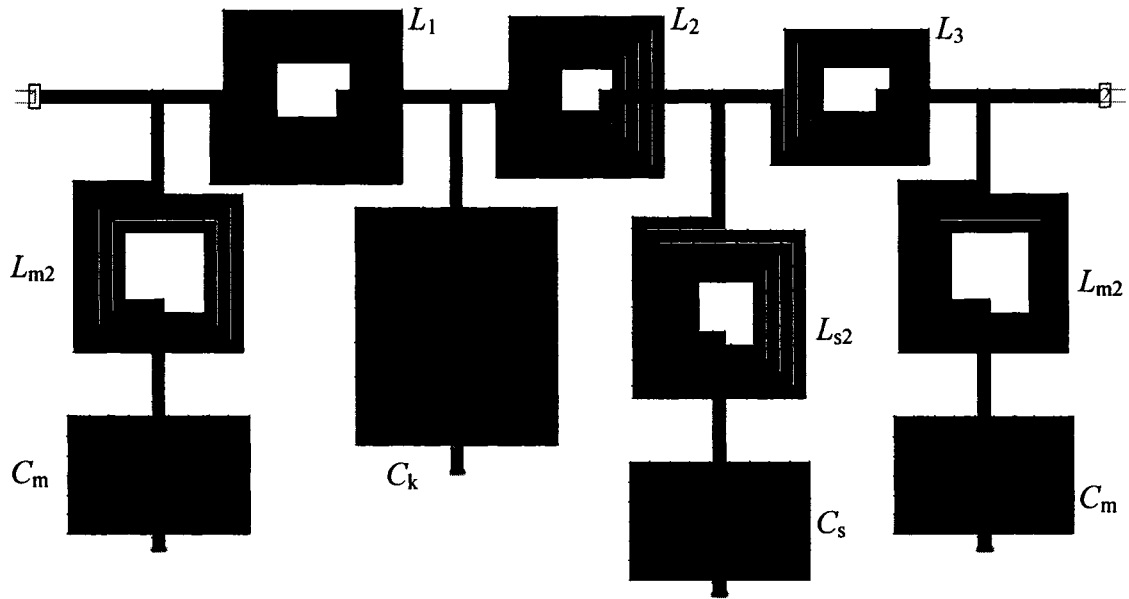


Figure 3.16 Layout of the proposed composite LPF in Zeland IE3D.

TABLE 3.3 DIMENSIONS OF SPIRAL INDUCTORS IN THE PROPOSED COMPOSITE LPF

Inductor	l (μm)	h (μm)	w (μm)	s (μm)	N
L_1	244	220	15	2	4.5
L_2	215	204	15	2	4.5
L_3	200	172	15	2	3.5
L_{m2}	219	216	15	2	3.5
L_{s2}	231	220	15	2	4.5

TABLE 3.4 DIMENSIONS OF MIM CAPACITORS IN THE PROPOSED COMPOSITE LPF

Capacitor	l (μm)	w (μm)
C_m	230	148
C_k	258	300
C_s	230	150

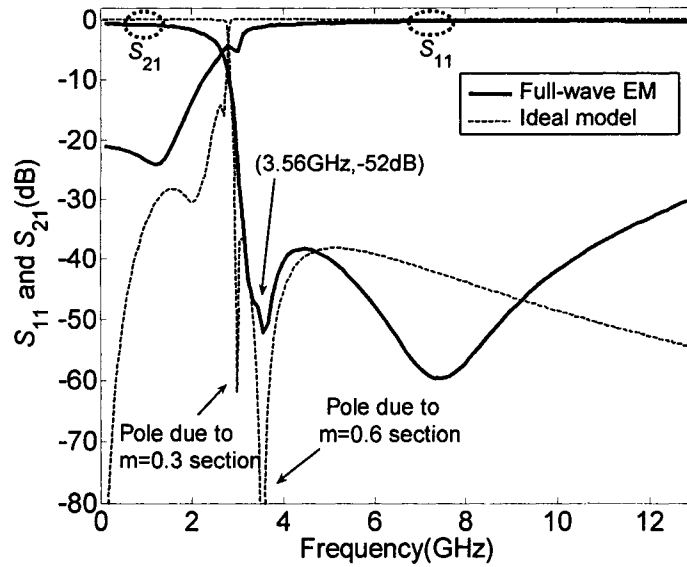


Figure 3.17 S -parameter responses of the proposed composite LPF obtained from EM simulations (Zeland *IE3D*) and ideal model simulations (Agilent *ADS*).

TABLE 3.5 COMPARISON OF THE PERFORMANCES OF THE PROPOSED FILTER OBTAINED USING IDEAL MODEL AND FULL-WAVE SIMULATIONS

	Loss at 0.19 GHz	f_c	f of 1 st pole	Attenuation of 1 st pole
Ideal model simulations	0 dB	2.8 GHz	3 GHz	-62 dB
Full-wave simulations	-0.76 dB	2.6 GHz	3.56 GHz	-52 dB

3.4 Summary

Planar compact LPFs having sharp cutoff are of increasing demand in many RF and microwave communication systems. In this chapter, an ultra compact planar composite LPF based on spiral inductors and MIM capacitors for MMIC applications has been presented. Besides exhibiting the desired cutoff frequency, the proposed LPF offers a flat pass-band, a sharp cutoff response, a low insertion loss in the passband, and a wide stopband. The size of the filter is considerably reduced compared to other filters operating in the same frequency range. This is achieved by first using a composite filter in the design process and second, realizing the circuit elements by using spiral inductors and MIM capacitors. A design procedure has been outlined so that the proposed design can be scaled to other frequencies. A comparison between EM simulations and ideal model responses has shown reasonable agreement.

Chapter 4

Nonlinear Circuit Simulation Using EM Coupling CAD Model

4.1 Background and Motivation

Electromagnetic (EM) coupling can be defined as electric/magnetic field interaction between two structures. In passive circuits, coupling takes the form as either mutual coupling or distributed coupling. Mutual coupling refers to the EM field interaction between two distinct components, such as between a resistor and a capacitor or between antenna elements [48]. Distributed coupling on the other hand, is EM field interactions involving distributed elements. In many cases, EM coupling can be a desirable behavior and is used in many distributed filters and couplers. Parasitic EM coupling on the other hand becomes a more serious concern in high frequency lumped circuit designs, especially where a circuit is dense and/or compact [27]. This is due to the fact that parasitic EM coupling can change the circuit response from what is expected and it can be complicated to evaluate [32][49]. This chapter focuses on parasitic EM coupling and a

technique to model the corresponding effects in the simulation process. Existing lumped or geometry-based models fail to account for full-wave EM effects at higher frequencies. On the other hand, commercial full-wave EM simulators (*e.g.* Ansoft *HFSS* [10], Sonnet *em* [11], Agilent Momentum [12]), based on Maxwell's theory tend to be accurate but require prohibitive computation-time and memory.

Considering the repetitive computations involved in simulation and optimization of modern RF/microwave integrated circuits (*e.g.* *Monte Carlo*), developing accurate and fast CAD models for full-wave EM characterization (including higher-order coupling) is of immense interest to RF/microwave designers. Some recent lumped EM-based models of passive components seem to be helpful in obtaining a quick initial design. However, such models are developed under perfectly shielded conditions excluding coupling between neighboring components, and hence tend to be inefficient for circuit-level simulation. For instance, EM-based neural models of passive components [50] have not accounted for coupling between neighboring modules. Quite recently, a novel EM coupling CAD modeling technique based on circuit theory and deembedding concepts [33] has been proposed [34]. Exploiting full-wave EM simulations/data from commercial EM solvers, this technique takes into account inter-component coupling. The accuracy and efficiency of the modeling technique has been demonstrated for a variety of passive circuits including series RLC and shunt RLC circuits, T-capacitive circuit, and band-pass filter.

Active devices (*e.g.* transistors) are widely used in RFICs (*e.g.* power amplifiers). In this chapter, the CAD modeling technique [34] is applied to nonlinear circuit simulation. More specifically, consideration is given to a power amplifier circuit consisting of both active devices and passive components. The circuit is divided into four sections. Two of the sections are purely passive, while two others consist of both active and passive modules (*e.g.* FET-stage including the bias circuit). First, EM coupling models of four sections are developed exploiting representative EM data from Agilent Momentum. Second, these sub-circuit models are combined or integrated for performing accurate and fast circuit-level simulations. The related work has already been published in [51].

4.2 Characteristic Matrices and their Properties

The EM coupling model to be discussed in section 4.3 is based on mathematical manipulations of both S - and T -matrices. As such, the basic properties of these characteristic matrices are presented here.

4.2.1 Scattering Parameter Matrices

An n -port network has n external connections into which power can be both fed in and out. Generally, power can get from any port (as input) to any other port (as output). Thus there are n incoming (incident) waves with complex amplitudes usually designated by the n complex quantities a_n , and n outgoing (reflected) waves with complex amplitudes designated by the n complex quantities b_n . A representation more in accord with direct measurements, and with the ideas of incident, reflected, and transmitted waves, is given

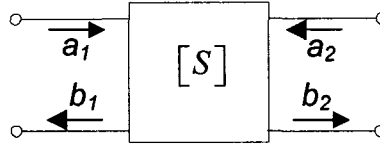


Figure 4.1 A two port network representation with the related incident and reflected waves.

by the scattering matrix. The scattering matrix $[S]$ relates the incident waves $[a]$ to the reflected waves $[b]$ by the following relation

$$\begin{bmatrix} b_1 \\ \vdots \\ b_n \end{bmatrix} = \begin{bmatrix} S_{11} & \cdots & S_{1n} \\ \vdots & \ddots & \vdots \\ S_{n1} & \cdots & S_{nn} \end{bmatrix} \begin{bmatrix} a_1 \\ \vdots \\ a_n \end{bmatrix} \quad (4.1)$$

where $[S]$ is an n -by- n square matrix of complex numbers whose elements are termed "S-parameters". A two-port network, showing the related incident and reflected waves is illustrated in Fig. 4.1.

4.2.2 Transfer Matrix

Any passive based n -port system can be defined as a combination of series and/or parallel individual devices. So its overall characteristic matrix can be conveniently obtained from the individual device matrices using the transfer scattering-parameters also known as the T -parameters [52][53]. As for the S -parameters, the T -parameters are defined as a function of the incident and reflected waves as

$$\begin{bmatrix} b_1 \\ a_1 \end{bmatrix} = \begin{bmatrix} T_{11} & T_{12} \\ T_{21} & T_{22} \end{bmatrix} \begin{bmatrix} a_2 \\ b_2 \end{bmatrix}. \quad (4.2)$$

The advantage of T -parameters compared to S -parameters is that they can be used to determine the effect of cascading two or more two-port networks by simply multiplying the associated individual T -parameter matrices. Let $[T_1]$, $[T_2]$ and $[T_3]$ be the T -parameters of three different two-port networks: the T -parameter matrix for the cascade of all three networks ($[T_T]$) in series is given by

$$[T_T] = [T_1] \times [T_2] \times [T_3]. \quad (4.3)$$

Relationships for converting S -parameters to T -parameters and vice-versa are given by the following equations [52]

$$T_{11} = \frac{-S_{11}S_{22} + S_{12}S_{21}}{S_{21}} \quad (4.4a)$$

$$T_{12} = \frac{S_{11}}{S_{21}} \quad (4.4b)$$

$$T_{21} = \frac{-S_{22}}{S_{21}} \quad (4.4c)$$

$$T_{22} = \frac{1}{S_{21}} \quad (4.4d)$$

and

$$S_{11} = \frac{T_{12}}{T_{22}} \quad (4.5a)$$

$$S_{12} = T_{11} - \frac{T_{12}T_{21}}{T_{22}} \quad (4.5b)$$

$$S_{21} = \frac{1}{T_{22}} \quad (4.5c)$$

$$S_{22} = -\frac{T_{21}}{T_{22}} \quad (4.5d)$$

4.3 Review of the Coupling Model Technique

This work is motivated by the EM coupling modeling technique of [34], which takes parasitic coupling into account. A brief review of the technique is presented below.

Consider two components, A and B , connected in series by a transmission line or interconnect I (see Fig. 4.2(a)). EM coupling between components, *i.e.* A and I , and I and B , can be accounted for by adding extra sub-networks X_1 and X_2 in series between components (see Fig. 4.2(b)). The T -parameter matrix of the overall circuit excluding and including coupling are expressed as

$$[T_{\text{without coupling}}] = [T_A] \times [T_I] \times [T_B] \quad (4.6)$$

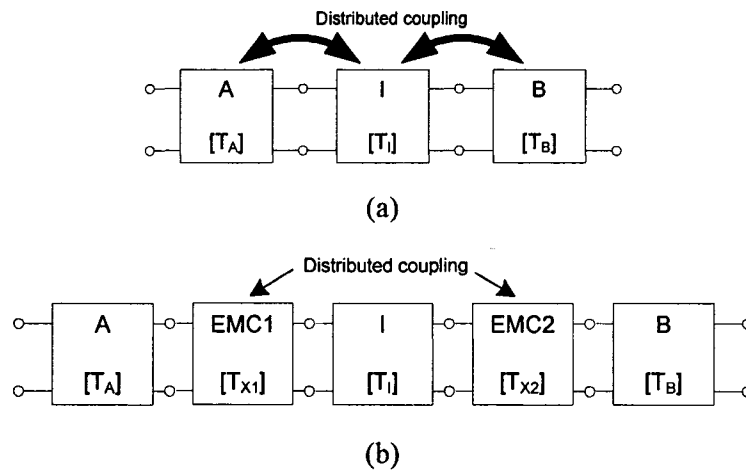


Figure 4.2 (a) Original circuit, in which, $[T_A]$ and $[T_B]$ are the transfer matrices of components A and B , respectively, and $[T_I]$ is the transfer matrix of interconnect I . (b) Modified topology [34], which includes EM coupling between components denoted by $[T_{X1}]$ and $[T_{X2}]$ respectively.

and

$$[T_{\text{with coupling}}] = [T_A] \times [T_{X1}] \times [T_I] \times [T_{X2}] \times [T_B]. \quad (4.7)$$

The algorithm for extracting coupling between components in series in terms of the T -parameters (ignoring coupling between far-away components A and B) is provided below.

Step 1 Simulate/measure the individual components including interconnects to obtain $[S_A]$, $[S_I]$ and $[S_B]$. Convert to T -parameters to obtain $[T_A]$, $[T_I]$ and $[T_B]$.

Step 2 Simulate/measure all possible combinations of these components (considering two at a time) to obtain $[S_{AI}]$ and $[S_{IB}]$. Convert to T -parameters to obtain $[T_{AI}]$ and $[T_{IB}]$. In theory, it should be noted that

$$[T_{AI}] = [T_A] \times [T_{X1}] \times [T_I] \quad (4.8)$$

and

$$[T_{IB}] = [T_I] \times [T_{X2}] \times [T_B]. \quad (4.9)$$

Step 3 Unknown couplings $[T_{X1}]$ and $[T_{X2}]$ are found using

$$[T_{X1}] = [T_A]^{-1} \times [T_{AI}] \times [T_I]^{-1} \quad (4.10)$$

and

$$[T_{X2}] = [T_I]^{-1} \times [T_{IB}] \times [T_B]^{-1}. \quad (4.11)$$

Step 4 Compute $[T_{\text{without coupling}}]$ and $[T_{\text{with coupling}}]$ using (4.6) and (4.7).

In general, a circuit under consideration can be divided into several sub-networks (or sections) in series, where each of the sub-sections can consist of one or more components. As mentioned earlier, the above algorithm has been demonstrated for a variety of passive circuits in [34]. One of those examples is presented here. Consider the series RLC circuit of Fig. 4.3. The circuit is built on a $120\ \mu\text{m}$ GaAs substrate ($\epsilon_r = 12.9$). The resistor is made from a $40\ \text{Ohm/Square}$ material with the area of $130\ \mu\text{m} \times 80\ \mu\text{m}$. The inductor has 4.5 turns with a line width of $10\ \mu\text{m}$, line spacing of $2\ \mu\text{m}$, and an inside square length of $30\ \mu\text{m}$. The capacitor has an area of $125\ \mu\text{m} \times 200\ \mu\text{m}$, where the distance between the plates is $1\ \mu\text{m}$. This passive circuit is divided into three sections, where each section simply consists of a component (*i.e.* R , L and C). EM data is obtained from a commercial Sonnet *em* simulator [11]. Inter-component EM coupling is computed employing the above steps. The approach leads to accurate circuit responses as shown in Fig. 4.4. Significant improvement in terms of computation-time (1s versus 1500s) is reported.

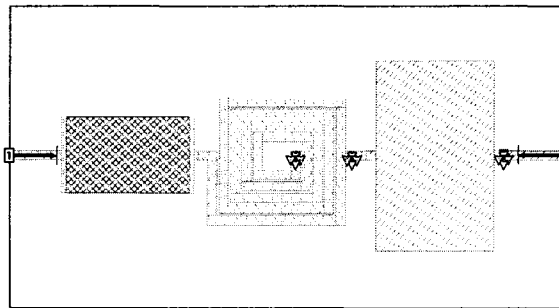


Figure 4.3 Series RLC circuit considered in [34] to demonstrate the usefulness of the coupling algorithm.

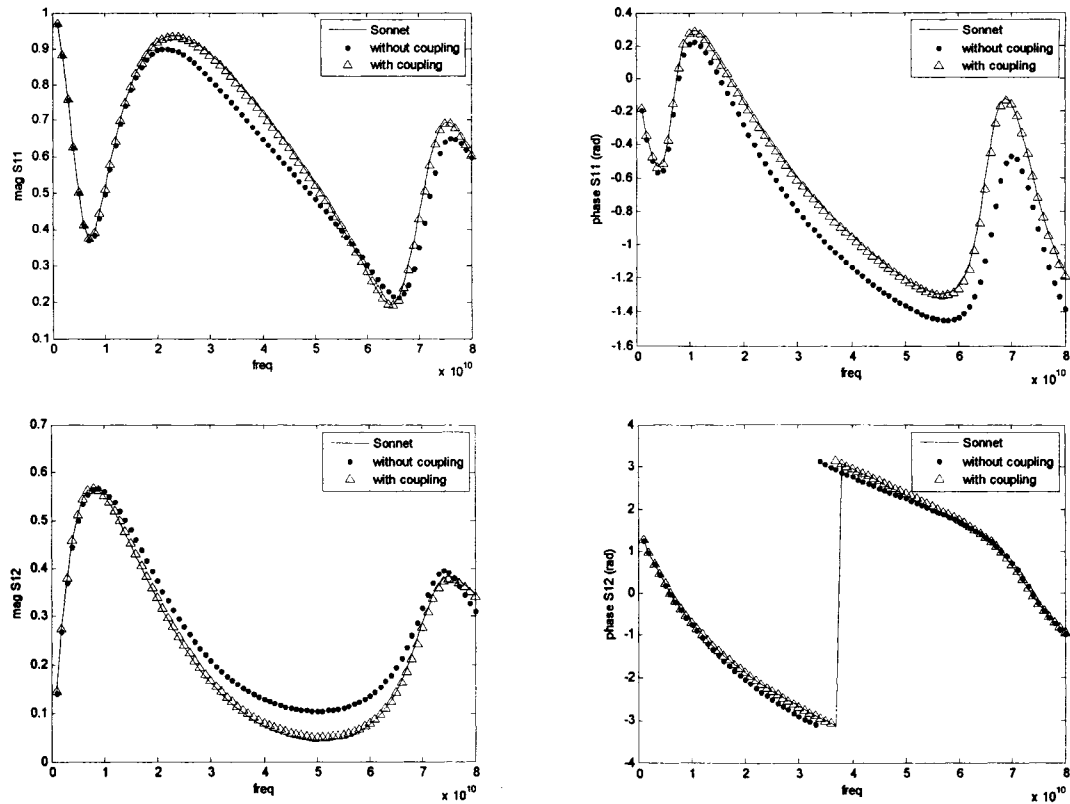


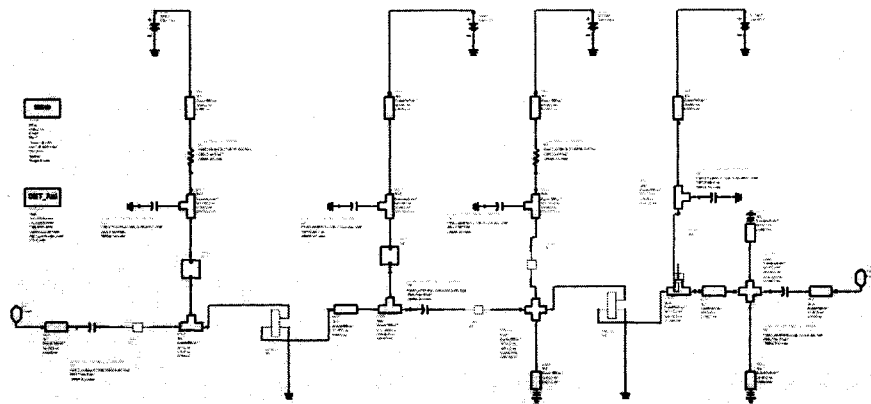
Figure 4.4 Comparison of magnitudes and phases of the scattering parameters S_{11} and S_{12} computed using the recent coupling algorithm [34] with those obtained from a time-consuming direct overall circuit simulation in Sonnet *em*.

4.4 Application to Nonlinear Simulation

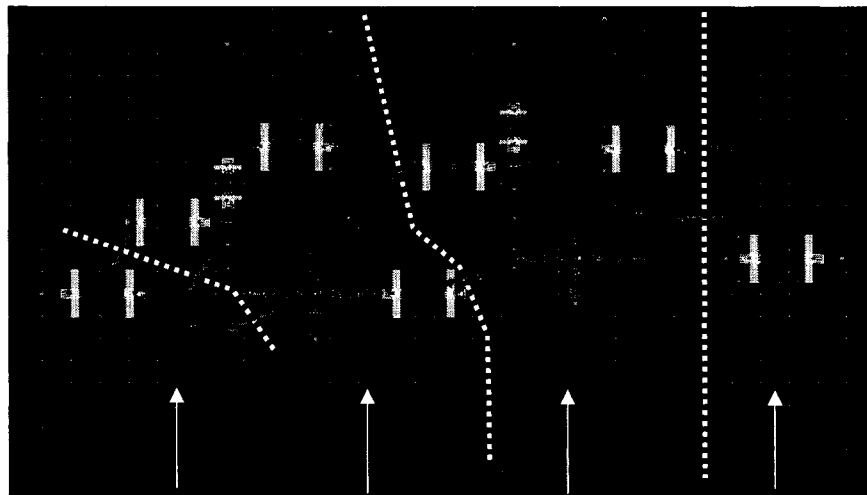
The presented work is based on the idea that if a given circuit includes “active devices”, division of the circuit into sections must be carried out such that each of the active devices and the corresponding bias networks stay together in the same section. Otherwise, the operating point of the active device in the separate section and in the

complete circuit will differ from each other. A cellular power amplifier circuit of Fig. 4.5(a), with its layout in Agilent Momentum [12] shown in Fig. 4.5(b), is studied. This circuit is available in the ADS example library. (Location: /examples/RF_Board/cellular_pamp_prj).

Agilent Momentum can only simulate passive components and not active components. Hence, the distributed passive components in the power amplifier circuit of Fig. 4.5(a) are simulated in Momentum. The resulting EM data of these distributed passive components are plugged into Agilent *ADS* schematic page by using “Layout Components” of Momentum. Layout Components are user-defined components that can be created from a layout in Momentum. They can be inserted in a schematic page just like any other component. When doing a circuit simulation from the schematic environment, the Momentum planar EM solver will be called automatically during the circuit simulation to generate a Momentum model for the layout components in the circuit [12]. Agilent *ADS* offers library models for active devices too, therefore, the total circuit containing both active and passive components can be simulated in the *ADS* schematic page while keeping the accuracy of EM simulation. A harmonic balance simulation of the overall circuit is performed within the Agilent *ADS* environment. The frequency spectra and the time-domain waveforms of the output signal corresponding to two different input power levels are shown in Fig. 4.6. Figure 4.7 shows the plot of output versus input powers. The results illustrate the nonlinear characteristic of the power amplifier.



(a)



Section 1 Section 2 Section 3 Section 4

(b)

Figure 4.5 (a) ADS schematic and (b) Momentum layout of the power amplifier.

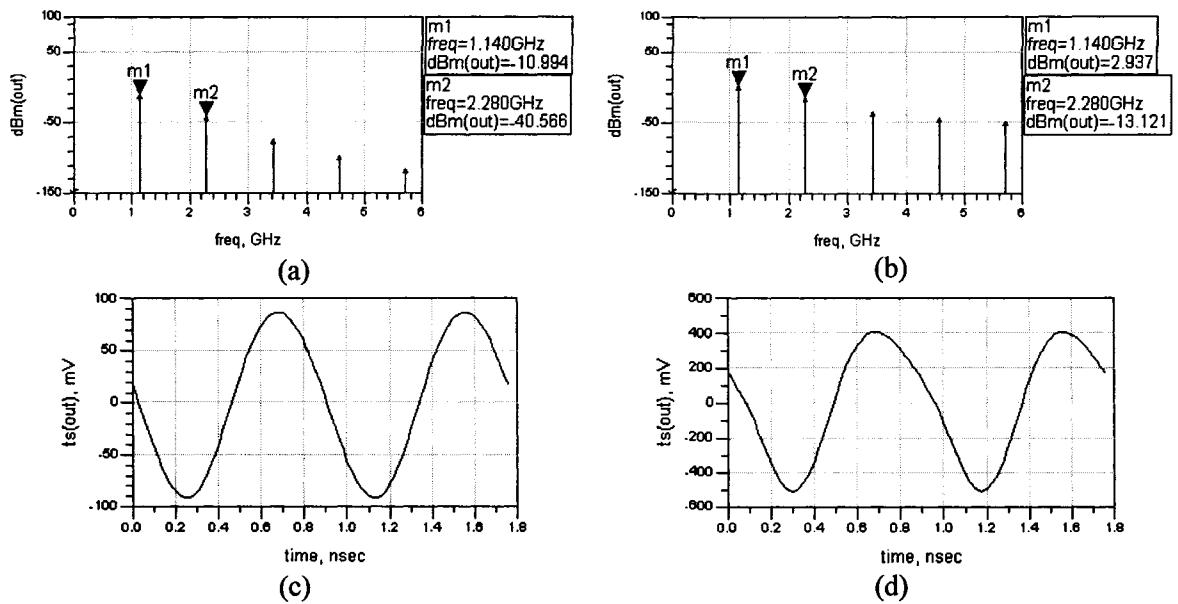


Figure 4.6 Frequency spectra of the output signal corresponding to (a) input power = -20dBm and (b) input power = -3 dBm. Time-domain waveforms of the output signal corresponding to (c) input power = -20dBm and (d) input power = -3dBm.

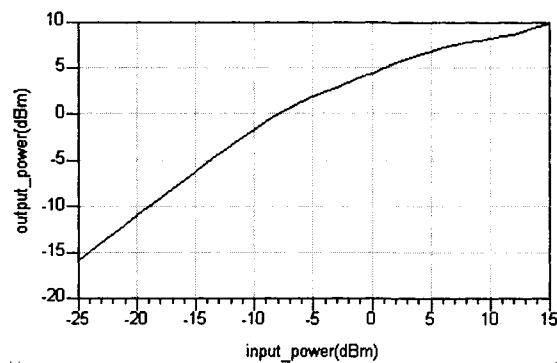


Figure 4.7 Output power *versus* input power of the power amplifier.

The coupling algorithm is then applied. As seen in Fig. 4.5(b), the overall circuit is divided into four sections. Such decomposition helped preserve the FET-stages and corresponding bias networks such that the operating points do not change. The locations at which EM coupling could be critical are highlighted using double-headed arrows.

Step 1 Sections 1 and 4 are simulated in Momentum. However, sections 2 and 3 contain FETs which are not supported by Momentum. First, distributed passive components of sections 2 and 3 are simulated in Momentum. EM data is plugged into the *ADS* schematic page by using “Layout Components” of Momentum. Then sections 2 and 3 including FETs are simulated in the *ADS* schematic page. *S*-parameters of four sections *i.e.* $[S_1], \dots[S_4]$ are obtained from simulation results and converted to *T*-parameters *i.e.* $[T_1], \dots[T_4]$.

Step 2 Considering two adjacent sections at a time leads to three combinations *i.e.* 1-2, 2-3, and 3-4. The two adjacent sections are connected and simulated in *ADS* to obtain *S*-parameters of three combinations. Then *S*-parameters are converted to *T*-parameters to obtain $[T_{12}]$, $[T_{23}]$, and $[T_{34}]$. (Note that $[T_{12}]$ is the *T*-parameters of the combination section 1-2)

Step 3 EM couplings between pairs of sections are computed in a manner similar to (4.10) and (4.11) by

$$[T_{X12}] = [T_1]^{-1} \times [T_{12}] \times [T_2]^{-1} \quad (4.12)$$

$$[T_{X23}] = [T_2]^{-1} \times [T_{23}] \times [T_3]^{-1} \quad (4.13)$$

$$[T_{X34}] = [T_3]^{-1} \times [T_{34}] \times [T_4]^{-1} \quad (4.14)$$

where $[T_{X12}]$, $[T_{X23}]$, and $[T_{X34}]$ are the EM coupling T -parameters between pairs of sections.

Step 4 Transfer matrices of the amplifier are computed in a manner similar to (4.6) and (4.7) by

$$[T_{\text{without coupling}}] = [T_1] \times [T_2] \times [T_3] \times [T_4] \quad (4.15)$$

$$[T_{\text{with coupling}}] = [T_1] \times [T_{X12}] \times [T_2] \times [T_{X23}] \times [T_3] \times [T_{X34}] \times [T_4]. \quad (4.16)$$

These matrices help to simulate the circuit both without and with coupling.

For the purpose of comparison, the overall circuit is simulated in *ADS* using “Layout Components” of Momentum. As seen from Fig. 4.8, the results of the algorithm show a good agreement with those from direct overall circuit simulation. This example shows the usefulness of the coupling algorithm in nonlinear CAD. From a RF/microwave perspective, direct overall circuit simulation is always CPU-intensive while “decomposed simulations” such as our work, are manageable. Subdividing a circuit to perform simulations more quickly is not a novel concept. However, by using coupling models, simulation accuracy is kept high by including the effects of coupling.

The advantage of the technique becomes more obvious, knowing that all the simulations required to calculate the coupling models can be performed off-line. This permits the creation of a library of components and/or sections to be used. Once implemented in a circuit simulator, the resulting simulation time is on the order of a

fraction of seconds. Moreover, because each component can be assumed to interact only with adjacent components, there is no need to re-simulate the entire network when only a single component is altered. Therefore, if it is necessary to consider more than one possible value for each component, this approach can provide enormous savings in time while maintaining reasonably accurate results. The obvious application of this approach is in optimization.

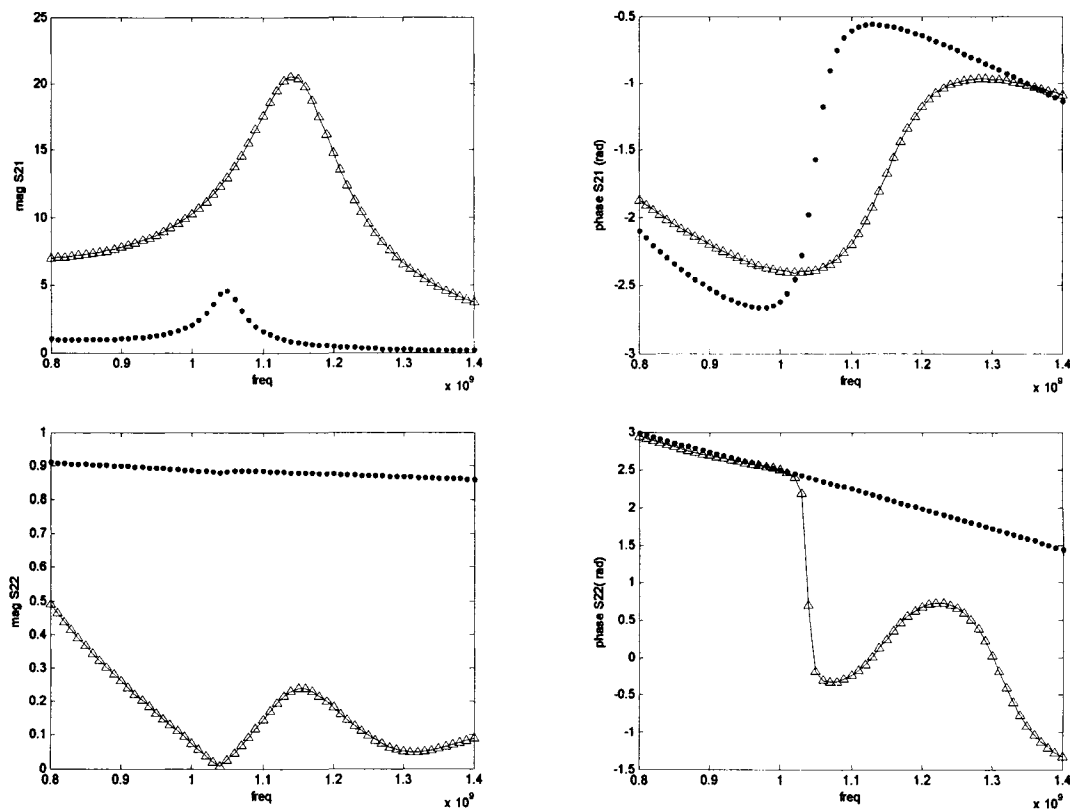


Figure 4.8 Comparison of magnitudes and phases of the scattering parameters S_{21} and S_{22} computed using the recent coupling algorithm both without coupling (.) and with coupling (Δ), with those obtained from time-consuming direct overall circuit-level simulation (—).

4.5 Summary

Since parasitic EM coupling can have a major effect on the circuit response, particularly at high frequencies, accurate modeling of this coupling is an important factor for efficient CAD of RFICs/MMICs. In this chapter, a recent technique for EM coupling modeling has been reviewed and for the first time, it has been applied to a nonlinear power amplifier circuit simulation. Such work is promising since it allows decomposed circuit simulations as alternatives to CPU-intensive overall circuit simulations. It also helps the design of microwave integrated circuits to be faster, more accurate and efficient, thereby contributing to overall reductions in design cycles.

Chapter 5

Conclusions

Higher integration and smaller layout size are two major trends in today's industry. As such, the research work in this thesis has been focused on compact design of inductors and LPFs, and modeling of parasitic EM coupling which is more of a concern in dense circuits.

In chapter 2, design/optimization of spiral inductors as a compact component level design has been studied. Higher integration can be achieved by using lumped elements such as spiral inductors, which are widely used as lumped elements in electronic circuits, *e.g.* LNAs, VCOs, and filters. Inductors with high Q are required to enhance the performance of these RF circuits. As such, CAD and optimization of on-chip spiral inductors are important. An implicit space mapping technique has been applied to the optimization of spiral inductors in chapter 2. Starting with user-specifications (*e.g.* those from an RFIC designer), the proposed algorithm yields a satisfactory EM-validated spiral inductor design using comparatively less EM data. Compared to traditional optimization methods, which are based on circuit models, considerable improvement has been

obtained in terms of accuracy. Compared to the recent space mapping algorithm for spiral inductor optimization based on geometric programming, the proposed space mapping algorithm in chapter 2 neither requires defining iteration-dependent constraints in the parameter extraction step nor involves any assumptions in terms of the format of the objective/constraint functions. Furthermore, the proposed algorithm needs less CPU-expensive EM data.

Future work in this area could be extending the applicability of the algorithm to spiral inductor optimization well above the currently demonstrated 3GHz frequency. Another direction is the application of the proposed technique to the circuit level optimization, *e.g.* optimization of VCOs and LNAs.

In chapter 3, design/optimization of composite LPFs as a compact circuit level design has been studied. Design of LPFs which are compact and exhibit sharper attenuation responses is challenging. Traditional approaches (*e.g.* Butterworth, Chebyshev, and Elliptic) entail higher-order topologies to achieve a flat passband and sharp attenuation, and hence directly contradict the design requirements. A composite LPF can be promising in such challenging scenarios. A composite LPF, which consists of four sections, namely: a constant- k , an m -derived sharp cutoff, and two m -derived matching sections, has been designed in chapter 3. Since microwave printed filters provide various advantages over waveguide and coaxial line filters, such as low weight, low cost, compact size and high accuracy, the designed composite LPF has been realized using spiral inductors and MIM capacitors. Besides exhibiting the desired cutoff frequency, the

proposed LPF offers a flat pass-band, a sharp cutoff response, a low insertion loss in the passband, and a wide stopband. The size of the filter is considerably reduced compared to other filters operating in the same frequency range. A design procedure has been outlined so that the proposed design can be scaled to other frequencies. A comparison between EM simulations and ideal model responses has shown reasonable agreement.

Finally, since higher integration leads to more prominent parasitic electromagnetic coupling effects in high-frequency communication systems, in chapter 4 of this thesis a technique to model these effects has been studied. For the first time, the technique has been applied to nonlinear circuit (a power amplifier) simulation. The power amplifier circuit has been divided into four sections. Two of the sections are purely passive, while two others consist of both active and passive modules (*e.g.* FET-stage including the bias circuit). First, EM coupling models of the four sections has been developed exploiting representative EM data from Agilent Momentum. Second, these sub-circuit models are combined or integrated for performing accurate and fast circuit-level simulations. Such work is promising since it allows decomposed circuit simulations as alternatives to CPU-intensive overall circuit simulations. It also helps making the design of microwave integrated circuits faster, more accurate and efficient, contributing to overall reductions in design cycles.

Future work can involve the application of the coupling models in circuit optimization. Such goal may include electrical as well as geometrical parameters. In fact, coupling models are uniquely suited to this application since they are well suited to generate large

ranges of data. Modifying the circuit parameters and/or the circuit configuration (topology) for smaller size and/or improved performance can be significantly accelerated using coupling models in comparison with an optimization round in a EM simulator. If a library of components with associated coupling models is available, then modifications can be performed almost instantly, as opposed to waiting for new full wave simulations. Due to its potential for time savings, this is an exciting area of research.

References

- [1] P. Sharma, F. Mohammadi, and M.C.E. Yagoub, "Neural design and optimization of RF/Microwave EM-based multichip modules," *Proc. RF and Microwave Conference*, Subang, Malaysia, Oct. 2004, pp. 67-71.
- [2] Y. Momiyama, T. Hirose, H. Kurata, K. Goto, Y. Watanabe, and T. Sugii, "A 140 GHz f_t and 60 GHz f_{max} DTMOS integrated with high-performance SOI logic technology," *Proc. Int. Electron Devices Meeting.*, San Francisco, CA, Dec. 2000, pp. 451-454.
- [3] A. Gruhle, "Prospects for 200 GHz on silicon with SiGe heterojunction bipolar transistors," *Proc. IEEE Bipolar/BiCMOS Circuits Technology Meeting*, Minneapolis, MN, Sep.-Oct. 2001, pp. 19-25.
- [4] J.N. Burghartz, D.C. Edelstein, M. Soyuer, H.A. Ainspan, and K.A. Jenkins, "RF circuit design aspects of spiral inductors on silicon," *IEEE J. Solid-State Circuits*, vol. 33, no. 12, pp. 2028-2034, Dec. 1998.
- [5] C.P. Yue, C. Ryu, J. Lau, T.H. Lee, and S.S. Wong, "A physical model for planar spiral inductors on silicon," *Proc. Int. Electron Devices Meeting*, San Francisco, CA, Dec. 1996, pp. 155-158.
- [6] C.P. Yue and S.S. Wong, "Physical modeling of spiral inductors on silicon," *IEEE Trans. on Electron Devices*, vol. 47, no. 3, pp. 560-568, Mar. 2000.
- [7] K.B. Ashby, I.A. Koullias, W.C. Finley, J.J. Bastek, and S. Moinian, "High Q inductors for wireless applications in a complementary silicon bipolar process," *IEEE J. Solid-State Circuits*, vol. 31, no. 1, pp. 4-9, Jan. 1996.

- [8] S.S. Mohan, M. Hershenson, S.P. Boyd, and T.H. Lee, "Simple accurate expressions for planar spiral inductances," *IEEE J. Solid-State Circuits*, vol. 34, no. 10, pp. 1419-1424, Oct. 1999.
- [9] J.R. Long and M.A. Copeland, "The modeling, characterization, and design of monolithic inductors for silicon RF IC's," *IEEE J. Solid-State Circuits*, vol. 32, no. 3, pp. 357-369, Mar. 1997.
- [10] Ansoft High Frequency Structure Simulator (*HFSS*) v.10.0, Ansoft Corp., 225 West Station Square Drive, Pittsburg, PA 15219.
- [11] Sonnet *em* 10.53, Sonnet Software, Inc. 100 Elwood Davis Road, North Syracuse, NY 13212, USA.
- [12] Agilent Momentum, Agilent Technologies, 1400 Fountaingrove Parkway, Santa Rosa, CA 95403-1799, USA.
- [13] C.-Y. Lee, T.-S. Chen, J.D.-S. Deng, and C.-H. Kao, "A simple systematic spiral inductor design with perfected Q improvement for CMOS RFIC application," *IEEE Trans. Microwave Theory Tech.*, vol. 53, no. 2, pp. 523-528, Feb. 2005.
- [14] M.D.M. Hershenson, S.S. Mohan, S.P. Boyd, and T.H. Lee, "Optimization of inductor circuits via geometric programming," *Proc. 36th Design Automation Conf.*, New Orleans, LA, Jun. 1999, pp. 994-998.
- [15] G. Stojanovic and L. Zivanov, "Comparison of optimal design of different spiral inductors," *24th Int. Conf. Microelectronics*, Nis, Serbia & Montenegro, May 2004, pp. 613-616.

- [16] Y. Zhan and S.S. Sapatnekar, "Optimization of integrated spiral inductors using sequential quadratic programming," *Proc. Design, Automation and Test in Europe Conf.*, Paris, France, Feb. 2004, pp. 622-627.
- [17] A. Nieuwoudt and Y. Massoud, "Multi-level approach for integrated spiral inductor optimization," *Proc. 42nd Design Automation Conf.*, Anaheim, California, Jun. 2005, pp. 648-651.
- [18] J.W. Bandler, R.M. Biernacki, S.H. Chen, P.A. Grobelny, and R.H. Hemmers, "Space mapping technique for electromagnetic optimization," *IEEE Trans. Microwave Theory Tech.*, vol. 42, no. 12, pp. 2536-2544, Dec. 1994.
- [19] J.W. Bandler, R.M. Biernacki, S.H. Chen, R.H. Hemmers, and K. Madsen, "Electromagnetic optimization exploiting aggressive space mapping," *IEEE Trans. Microwave Theory Tech.*, vol. 43, pp. 2874-2882, 1995.
- [20] M.H. Bakr, J.W. Bandler, N.K. Georgieva, and K. Madsen, "A hybrid aggressive space-mapping algorithm for EM optimization," *IEEE Trans. Microwave Theory Tech.*, vol. 47, pp. 2440-2449, 1999.
- [21] J.W. Bandler, Q.S. Cheng, N.K. Nikolova, and M.A. Ismail, "Implicit space mapping optimization exploiting preassigned parameters," *IEEE Trans. Microwave Theory Tech.*, vol. 52, pp. 378-385, 2004.
- [22] J.W. Bandler, Q.S. Cheng, D. Gebre-Mariam, K. Madsen, F. Pedersen, and J. Søndergaard, "EM-based surrogate modeling and design exploiting implicit, frequency and output space mappings," *IEEE MTT-S Int. Microwave Symp. Dig.*, Philadelphia, PA, 2003, pp. 1003-1006.

- [23] J.W. Bandler, Q. Cheng, S.A. Dakroury, A.S. Mohamed, M.H. Bakr, K. Madsen, and J. Søndergaard, "Space mapping: the state of the art," *IEEE Trans. Microwave Theory Tech.*, vol. 52, pp. 337-361, 2004.
- [24] G. Matthaei, L. Young, and E.M.T. Jones, *Microwave Filters, Impedance-Matching Networks, and Coupling Structures*, Norwood, MA: Artech House, 1980.
- [25] D.M. Pozar, *Microwave Engineering*, New York, NY: John Wiley & Sons, 2005.
- [26] M.C.E. Yagoub and P. Sharma, "Characterization of EM effects in RF/microwave integrated circuits," *34th European Microwave Conf.*, Amsterdam, Netherlands, Oct. 2004, pp. 221-224.
- [27] J.M. Dunn, L.C. Howard, and K. Larson, "An efficient algorithm for the calculation of parasitic coupling between lines in MIC's," *IEEE Trans. On Microwave Theory Tech*, vol. 41, pp. 1287-1293, 1993.
- [28] T.Dickson, M.LaCroix, S.Boret, D.Gloria, R.Beerkens, and S.Voinigescu, "30-100-GHz inductors and transformers for millimeter-wave (Bi)CMOS integrated circuits," *IEEE Trans. On Microwave Theory and Tech.*, vol. 53, pp. 123-133, Jan. 2005.
- [29] M. Gordon and S. Voinigescu, "An inductor-based 52-GHz 0.18 um SiGe HBT cascode LNA with 22 dB gain," *Proc. IEEE 30th European Solid-State Circuits Conference*, Leuven, Belgium, Sep. 2004, pp. 287-290.
- [30] M. Goldfarb and A. Platzker, "The effects of electromagnetic coupling on MMIC design," *Microwave & Millimeter Wave CAE*, vol. 1, pp. 38-47, 1991.
- [31] X. Ding, B. Chattaraj, M.C.E. Yagoub, V.K. Devabhaktuni, and Q.J. Zhang, "EM based statistical design of microwave circuits using neural models," *Int. Symp. on Microwave and Optical Technology*, Montreal, Canada, June 2001, pp. 421-426.

- [32] H. Baudrand, "Electromagnetic study of coupling between active and passive circuits," *Int. Microwave and Optoelectronics Conf.*, Natal, Brazil, Aug. 1997, pp. 143-152.
- [33] C. Chen and M. Deen, "A general noise and S-parameter deembedding procedure for on-wafer high-frequency noise measurements of MOSFETs," *IEEE Trans. On Microwave Theory Tech.*, vol. 49, pp. 1004-1005, 2001.
- [34] D. McPhee and M.C.E. Yagoub, "New technique for efficient computation of electromagnetic coupling," *Proc. IEEE MTT-S Int. Microwave Symp.*, San Francisco, CA, June 2006, pp. 1081-1084.
- [35] A.M. Niknejad, "Analysis, simulation, and applications of passive devices on conductive substrate," *Ph.D. Thesis*, Department of EECS, University of California, Berkeley, CA, Spring 2000.
- [36] W. Yu, "Optimization of spiral inductors and LC resonators exploiting space mapping technology," *M.Sc. Thesis*, Department of ECE, McMaster Univ., 1280 Main St. W., Hamilton, Canada, June 2006.
- [37] N. Arbabi, M. Najmabadi, M. Yagoub, and V. Devabhaktuni, "A new SQP based space-mapping algorithm for on-chip spiral inductor optimization," *Proc. CCECE*, Vancouver, Canada, April 2007, pp. 99-102.
- [38] K. Okada, H. Hoshino, and H. Onodera, "Modeling and optimization of on-chip spiral inductor in S-parameter domain," *Proc. Int. Symp. Circuits Systems*, Vancouver, Canada, May 2004, pp. 153-156.
- [39] H.G. Booker, *Energy in Electromagnetism*, London/New York: Peter Peregrinus (on behalf of the IEE), 1982.

- [40] C. Yue and S. Wong, "On-chip spiral inductors with patterned ground shields for Si-based RF IC's," *IEEE J. Solid-State Circuits*, vol. 33, pp. 743-752, 1998.
- [41] S.N. Uysal, "A compact coplanar stripline lowpass filter," *Asia-Pacific Microwave Conf. Dig.*, Westin Stamford & Westin Plaza, Singapore, Nov.-Dec. 30-2, 1999, vol. 2, pp. 307-310.
- [42] R.N. Martins and H. Abdalla, "Design of low-pass microstrip filters with equal-ripple passband and finite attenuation poles," *IEEE MTT-S Int. Microwave Optoelectronics Conf. Dig.*, Belem, Brazil, Aug. 6-10, 2001, vol. 1, pp. 71-74.
- [43] J.-S. Lim, C.-S. Kim, Y.-T. Lee, D. Ahn, and S. Nam, "Design of lowpass filters using defected ground structure and compensated microstrip line," *Electronics Letters*, vol. 38, pp. 1357-1358, October 2002.
- [44] C.-Y. Hung, R.-Y. Yang, M.-H. Weng, and Y.-K. Su, "A compact semi-lumped coplanar waveguide low-pass filter fabricated on high resistivity silicon substrate," *IEICE Trans. Electron.*, vol. 90, pp. 1837-1840, 2007.
- [45] I.J. Bahl, *Lumped Elements for RF and Microwave Circuits*, Norwood, MA: Artech House, 2003.
- [46] Z.D. Tan, J.S. Mandeep, S.I.S. Hassan, and M.F. Ain, "Composite low pass filter design with T and π network on microstrip line," *Microwave Journal*, vol. 50, pp. unavailable, Aug. 2007.
- [47] N. Arbabi, V. Devabhaktuni, and M.C.E. Yagoub, "A compact composite low-pass filter based on spiral inductors and MIM capacitors", *IEEE. Microwave and Wireless Component Lett.*, 2008. (pending)

- [48] M. Ozdemir, H. Arslan, and E. Arvas, "Mutual coupling effect in multiantenna wireless communication systems," *IEEE GLOBECOM Global Telecommunications Conference*, San Francisco, CA, November 2003, pp. 829-833.
- [49] W.Y. Yin, S.J. Pan, L.W. Li, and Y.B. Gan, "Experimental characterization of coupling effects between two on-chip neighboring square inductors," *IEEE Trans. EM Compatibility*, vol. 45, pp. 557-561, 2003.
- [50] X. Ding, V. Devabhaktuni, B. Chattaraj, M.C.E. Yagoub, M. Deo, J. Xu, and Q.J. Zhang, "Neural network approaches to electromagnetic-based modeling of passive components and their applications to high-frequency and high-speed nonlinear circuit optimization," *IEEE Trans. Microwave Theory Tech.*, vol. 52, pp. 436-449, 2004.
- [51] N. Arbabi, V. Devabhaktuni, and M.C.E. Yagoub, "Application of EM coupling CAD model to nonlinear integrated circuit simulation", *Asia-Pacific Microwave Conference (APMC)*, Bangkok, Thailand, Dec. 2007.
- [52] K.C. Gupta, R. Garg, and R. Chadha, *Computer aided design of microwave circuits*, Artech House, Dedham 1981.
- [53] D.A. Frickey, "Conversions between S, Z, Y, h, ABCD, and T parameters which are valid for complex source and load impedances," *IEEE Trans. Microwave Theory Tech.*, vol. 42, pp. 205-211, 1994.